

1 **Crustal Radial Anisotropy Across Eastern Tibet and the Western**
2 **Yangtze Craton**

3 Jiayi Xie¹, Michael H. Ritzwoller¹, Weisen Shen¹, Yingjie Yang², Yong Zheng³, and
4 Longquan Zhou⁴

5 1 – Center for Imaging the Earth’s Interior, Department of Physics, University of
6 Colorado at Boulder, Boulder, CO, 80309, USA (jiayi.xie@colorado.edu)

7 2 – Department of Earth and Planetary Sciences, Macquarie University, 2109, Sydney
8 Australia

9 3 – State Key Laboratory of Geodesy and Earth’s Dynamics, Institute of Geodesy and
10 Geophysics, CAS, Wuhan, 430077, China

11 4 - China Earthquake Network Center, Beijing, 100045, China

12 **Abstract**

13 Phase velocities across eastern Tibet and surrounding regions are mapped using Rayleigh
14 (8-65 sec) and Love (8-44 sec) wave ambient noise tomography using data from more
15 than 400 PASSCAL and CEArray stations. A Bayesian Monte-Carlo inversion method is
16 applied to generate 3-D distributions of Vsh and Vsv in the crust and uppermost mantle
17 from which radial anisotropy and isotropic Vs are estimated. Each distribution is
18 summarized with a mean and standard deviation, but is also used to identify “highly
19 probable” structural attributes, which include (1) positive mid-crustal radial anisotropy
20 ($V_{sh} > V_{sv}$) across eastern Tibet (spatial average = $4.8\% \pm 1.4\%$) that terminates
21 abruptly near the border of the high plateau, (2) weaker ($-1.0\% \pm 1.4\%$) negative radial
22 anisotropy ($V_{sh} < V_{sv}$) in the shallow crust mostly in the Songpan-Ganzi terrane, (3)
23 negative mid-crustal anisotropy ($-2.8\% \pm 0.9\%$) in the Longmenshan region, (4) positive
24 mid-crustal radial anisotropy ($5.4\% \pm 1.4\%$) beneath the Sichuan Basin, and (5) low Vs in
25 the middle crust (3.427 ± 0.050 km/s) of eastern Tibet. Mid-crustal $V_s < 3.4$ km/s
26 (perhaps consistent with partial melt) is highly probable only for three distinct regions:
27 the northern Songpan-Ganzi, the northern Chuandian, and part of the Qiangtang terranes.
28 Mid-crustal anisotropy provides evidence for sheet silicates (micas) aligned by
29 deformation with a largely horizontal foliation plane beneath Tibet and the Sichuan Basin
30 and a largely vertical foliation plane in the Longmenshan region. Near vertical cracks or
31 faults are believed to cause the negative anisotropy in the shallow crust underlying Tibet.

32
33
34
35
36
37
38
39

1. Introduction

40
41 Seismic shear waves that are horizontally polarized may travel with a different speed
42 (V_{sh}) from that of vertically polarized waves (V_{sv}). This difference in wave speed is
43 referred to as radial anisotropy, which is commonly represented as the percentage
44 difference between V_{sh} and V_{sv} in the medium: $(V_{sh}-V_{sv})/V_s$. In this case, V_s is
45 computed from V_{sh} and V_{sv} via a Voigt-average, $V_s = \sqrt{(2V_{sv}^2 + V_{sh}^2)/3}$ [Babuška,
46 1991], where V_s is the isotropic or effective shear wave speed of the medium.

47 The direct observation of radial anisotropy with regionally propagating shear waves,
48 which are confined to the crust and uppermost mantle, is extremely difficult. Thus, the
49 existence of radial anisotropy is typically inferred from observations of a period-
50 dependent discrepancy between the phase or group speeds of Rayleigh and Love waves.
51 The discrepancy is identified by the inability of a simply parameterized isotropic shear
52 velocity model to fit the dispersion characteristics of both types of waves simultaneously.
53 Observations of this Rayleigh-Love discrepancy attributed to radial anisotropy in the
54 mantle in which $V_{sh} > V_{sv}$ date back about half a century [Aki, 1964; Aki and
55 Kaminuma, 1963; McEvelly, 1964; Takeuchi et al., 1968]. Much more recently, radial
56 anisotropy in the uppermost mantle has been mapped worldwide [Montagner and
57 Tanimoto, 1991; Trampert and Woodhouse, 1995; Babuška et al., 1998; Ekström and
58 Dziewonski, 1998; Shapiro and Ritzwoller, 2002; Nettles and Dziewoński, 2008], and
59 there have also been inroads made into mapping radial anisotropy in the crust beneath the
60 US [Bensen et al., 2009; Moschetti and Yang, 2010; Moschetti et al., 2010] and Tibet
61 [Shapiro et al., 2004; Chen et al., 2010; Duret et al., 2010; Huang et al., 2010]. The
62 observations in Tibet are part of the steady improvement in the reliability and the lateral
63 and radial resolutions of surface wave dispersion studies that cover all [Ritzwoller et al.,

64 1998; *Villaseñor et al.*, 2001; *Levshin et al.*, 2005; *Maceira et al.*, 2005; *Caldwell et al.*,
65 2009; *Acton et al.*, 2010; *Yang et al.*, 2010, 2012] or parts of the high plateau [*Levshin et*
66 *al.*, 1994; *Cotte et al.*, 1999; *Rapine et al.*, 2003; *Yao et al.*, 2008, 2010; *Guo et al.*, 2009;
67 *Li et al.*, 2009; *Jiang et al.*, 2011; *Zhou et al.*, 2012].

68 The observation of crustal radial anisotropy has been taken as evidence for the existence
69 of strong elastically anisotropic crustal minerals aligned by strains associated with
70 processes of deformation [*Shapiro et al.*, 2004; *Moschetti et al.*, 2010]. Many continental
71 crustal minerals are strongly anisotropic as single crystals [*Barruol and Mainprice*, 1993;
72 *Mahan*, 2006], but some of the most common minerals (e.g., feldspars, quartz) have
73 geometrically complicated anisotropic patterns that destructively interfere within
74 polycrystalline aggregates [*Lloyd et al.*, 2009; *Ward et al.*, 2012]. Micas and amphiboles
75 are exceptions that exhibit more robust alignment in both crystallographic direction and
76 shape that produce simple patterns of seismic anisotropy [*Tatham et al.*, 2008; *Lloyd et*
77 *al.*, 2009]. For this reason, recent observations of strong anisotropy in the middle crust
78 have been attributed to the crystallographic preferred orientation (CPO) of mica
79 [*Nishizawa and Yoshino*, 2001; *Shapiro et al.*, 2004; *Moschetti et al.*, 2010]. In the lower
80 crust, amphibole may also be an important contributor to seismic anisotropy [*Kitamura*,
81 2006; *Barberini et al.*, 2007; *Tatham et al.*, 2008].

82 *Shapiro et al.* [2004] showed that crustal radial anisotropy is strong in western Tibet and
83 may extend into eastern Tibet where the resolution of their study was weaker.

84 Subsequently, *Duret et al.* [2010] presented evidence from individual seismograms using
85 aftershocks of the Wenchuan earthquake of 12 May 2008 that the Rayleigh-Love
86 discrepancy is so significant for paths crossing Tibet that crustal radial anisotropy

87 probably also extends into eastern Tibet. *Huang et al.* [2010] confirmed this expectation
88 by mapping crustal radial anisotropy in far southeastern Tibet. Example cross-
89 correlations of ambient noise for a path in the Qiangtang terrane (Figure 1) contain
90 Rayleigh and Love waves as shown in Figure 2a. Figure 2b illustrates that a Rayleigh-
91 Love discrepancy exists for this path, revealing that crustal radial anisotropy, indeed, is
92 present between stations located within eastern Tibet.

93 The objective of this paper is to map crustal radial anisotropy across all of eastern Tibet
94 (Figure 1), extending the results into adjacent areas north and east of the high plateau for
95 comparison. Rayleigh and Love wave phase velocity curves are measured from ambient
96 noise cross-correlations between each pair of simultaneously operating stations between 8
97 and 44 sec period for Love waves and 8 and 65 sec for Rayleigh waves. As shown later,
98 the inability for ambient noise to produce longer period Love wave measurements implies
99 that radial anisotropy cannot be reliably mapped deeper than about 50 km, which means
100 that we cannot place tight constraints on the strength of radial anisotropy in the
101 lowermost crust beneath Tibet. For this reason, we focus discussion on mid-crustal radial
102 anisotropy.

103 The inversion of surface wave data for a 3-D radially anisotropic shear wave speed model
104 consists of two stages: first, a tomographic inversion of measured Rayleigh and Love
105 wave dispersion curves for phase speed maps on a $0.5^\circ \times 0.5^\circ$ grid using the tomographic
106 method of *Barmin et al.* [2001] with uncertainties estimated using eikonal tomography
107 [*Lin et al.*, 2009] (Section 2), and second, a Bayesian Monte Carlo inversion [*Shen et al.*,
108 2013b] for a 3-D radially anisotropic shear velocity (V_{sv} , V_{sh}) model of the crust
109 (Section 3). The inversion estimates the posterior distribution of accepted models at each

110 location, which is used in two ways. First, at each grid node we summarize the
111 distribution at each depth with its mean and standard deviation. Using the mean of the
112 distribution, we show that strong mid-crustal positive ($V_{sh} > V_{sv}$) radial anisotropy is
113 observed across all of eastern Tibet and terminates abruptly as the border of the high
114 plateau is reached. It is also observed in the middle crust beneath the Sichuan Basin.
115 Negative anisotropy ($V_{sv} > V_{sh}$) is observed in the shallow crust beneath eastern Tibet
116 and in the middle crust of the Longmenshan region. Second, we also query the entire
117 distribution of models in order to determine which structural attributes are highly
118 probable, which are only likely, and which are prohibited. Throughout, we attempt to
119 address how uncertainties in prior knowledge (e.g., V_p/V_s in the crust) affect the key
120 inferences. Finally, we ask how the observations reflect on the presence or absence of
121 pervasive partial melt in the middle crust across Tibet and speculate on the physical
122 causes of several observed radial anisotropy features.

123 **2. Data processing and tomography**

124 **2.1 Love wave and Rayleigh wave tomography**

125 For Love wave data processing, we apply the procedure described by *Bensen et al.* [2007]
126 and *Lin et al.* [2008] to recordings at 362 stations (Figure 1), consisting of 180
127 PASSCAL and GSN stations and 182 Chinese Earthquake Array (CEArray) stations
128 [*Zheng et al.*, 2010]. We downloaded all available horizontal component data for
129 PASSCAL and GSN stations between years 2000 and 2011 from the IRIS DMC.
130 Horizontal component data for the CEArray stations were acquired in the years 2007
131 through 2009. We cut horizontal component ambient noise records into 1-day long time
132 series and then cross-correlate the transverse components (T-T) between all possible

133 station pairs, after the performance of the time domain and frequency domain
134 normalization procedures described by *Bensen et al.* [2007]. As *Lin et al.* [2008] showed,
135 Love wave energy dominates transverse-transverse (T-T) cross-correlations. After the
136 cross-correlations, we applied automated frequency-time analysis (FTAN; [*Bensen et al.*,
137 2007]) to produce Love wave phase speed curves for periods between 8 and 30 to 50 sec
138 (depending on the signal-to-noise ratio) for each station pair.

139 Rayleigh wave phase speed measurements are obtained from cross-correlations of
140 vertical-component ambient noise, the vertical-vertical (Z-Z) cross-correlations, which
141 are rich in Rayleigh waves. *Yang et al.* [2010] generated Rayleigh wave phase velocity
142 maps from ambient noise across the Tibetan Plateau. Instead of using their dispersion
143 maps directly, we re-selected the measurements for stations within our study region and
144 re-performed the tomography as described below. Example T-T and Z-Z cross-
145 correlations and measured phase speeds between the station-pair X4.D26 and X4.F17 are
146 shown in Figure 2.

147 For dispersion measurements at different periods, we exploited three criteria to identify
148 reliable measurements: (1) the distance between two stations must be greater than two
149 wavelengths to ensure sufficient separation of the surface wave packet from precursory
150 arrivals and noise and to satisfy the far-field approximation; (2) measurements must have
151 a signal-to-noise ratio (SNR) > 10 to ensure the reliability of the signal; and (3) the
152 observed travel times and those predicted from the associated phase velocity map
153 between each accepted station-pair must agree within a specified tolerance [*Zhou et al.*,
154 2012]. We found that horizontal components are problematic (mainly relative to criterion
155 (3) above) for 61 stations. Their removal left us with the 362 stations shown in Figure 1.

156 The vertical components of 26 stations are similarly identified as problematic and are
157 rejected from further analysis leaving 406 stations from which we obtain Rayleigh wave
158 measurements. This procedure produces about 30,000 Love wave phase velocity curves
159 and 40,000 Rayleigh wave curves.

160 Because eikonal tomography [*Lin et al.*, 2009] models off-great circle propagation, it
161 would be preferable to straight ray tomography [*Barmin et al.*, 2001]. Eikonal
162 tomography works best, however, where there are no spatial gaps in the array of stations.
163 There are gaps in our station coverage near 33°N, 100°E in eastern Tibet (Figure 1b).
164 Thus, we apply straight-ray tomography [*Barmin et al.*, 2001] to generate phase velocity
165 maps, but use eikonal tomography to estimate uncertainties in these maps, as described in
166 Section 2.2. To reduce the effect of non-ideal azimuthal coverage at some locations, we
167 simultaneously estimate azimuthal anisotropy, but these estimates are not used here.
168 What results are Love wave phase velocity maps ranging from 8 to 44 sec and Rayleigh
169 wave phase velocity maps from 8 to 65 sec period. Above 44 sec period, the SNR of
170 Love waves decreases dramatically, which degrades the ability to produce reliable high-
171 resolution maps. Examples of Rayleigh and Love wave phase speed maps at periods of
172 10 and 40 sec are shown in Figure 3. At 10 sec period, the maps are quite sensitive to
173 shallow crustal structures to about 20 km depth including the existence of sediments, and
174 at 40 sec period the maps are predominantly sensitive to structures near the Moho such as
175 crustal thickness.

176 **2.2 Uncertainties and local dispersion curves**

177 Local uncertainty estimates for each of the phase speed maps provide the uncertainties
178 used in the inversion for 3-D structure. Estimates of uncertainties in the Rayleigh and

179 Love wave phase speed maps are determined by eikonal tomography [*Lin et al.*, 2009],
180 which, as discussed above, does not produce uniformly unbiased phase speed estimates
181 where there are gaps in station coverage. We find, however, that it does produce reliable
182 uncertainty estimates, even in the presence of spatial gaps. Averaging the one-standard
183 deviation uncertainty maps across the study region, average uncertainties are found to
184 range between 0.012 to 0.057 km/s for Rayleigh waves and 0.016 to 0.060 km/s for Love
185 waves (Figure 4), minimize between about 12 and 25 sec period, and increase at both
186 shorter and longer periods. Because of the lower SNR and the fewer number of Love
187 wave measurements, uncertainties for Love waves tend to be larger than for Rayleigh
188 waves. In addition, the SNR decreases faster at long periods for Love waves than
189 Rayleigh waves, so the uncertainty for Love waves at long periods is higher still than for
190 Rayleigh waves. Uncertainties for both wave types increase toward the borders of the
191 maps at all periods.

192 Having estimated maps of period-dependent dispersion and uncertainty, local Rayleigh
193 and Love wave dispersion curves with associated uncertainties are generated on a
194 $0.5^\circ \times 0.5^\circ$ grid across the study region. These data are the input for the 3-D model
195 inversion that follows.

196 **3. Bayesian Monte Carlo inversion of local dispersion curves**

197 **3.1 Model parameterization and prior constraints**

198 The 3-D model comprises a set of 1-D models situated on a $0.5^\circ \times 0.5^\circ$ grid. Following
199 *Shen et al.* [2013a, 2013b], each of the 1-D models is parameterized with three principal
200 layers: a sedimentary layer, a crystalline crustal layer, and a mantle layer to a depth of
201 200 km. The sedimentary layer is isotropic and is described by two parameters: layer

202 thickness and constant shear wave speed V_s . Anisotropy in the sedimentary layer is
203 physically possible, but with the data used here cannot be resolved from anisotropy in the
204 crystalline crust. For this reason, we include anisotropy only below the sediments. The
205 crystalline crustal layer is described by nine parameters: layer thickness, five B-splines
206 (1-5) for V_{sv} (Figure 5), and three more independent B-splines for V_{sh} (2-4). We set V_{sh}
207 = V_{sv} for B-splines 1 and 5. Because B-splines 2 and 4 extend into the uppermost and
208 lowermost crust, respectively, radial anisotropy can extend into these regions but its
209 amplitude will be reduced relative to models in which V_{sh} and V_{sv} for B-splines 1 and 5
210 are free. The effect of this constraint is discussed in Section 5.4.1.

211 Mantle structure is modeled from the Moho to 200 km depth with five B-splines for V_{sv} .
212 V_{sh} in the mantle differs from V_{sv} by the depth-dependent strength of radial anisotropy
213 taken from the 3-D model of *Shapiro and Ritzwoller* [2002]. Thus, in the mantle we
214 estimate V_{sv} , but set $V_{sh} = V_{sv} + dV$ where dV is the difference between V_{sh} and V_{sv}
215 in the model of *Shapiro and Ritzwoller* [2002]. Below 200 km the model reverts to the
216 1D model ak135 [*Kennett et al.*, 1995]. The effect on estimates of crustal anisotropy
217 caused by fixing the amplitude of mantle anisotropy is considered in Section 5.4.2.

218 Overall, there are 16 free parameters at each point and the model parameterization is
219 uniform across the study region.

220 Because Rayleigh and Love wave velocities are mainly sensitive to shear wave speeds,
221 other variables in the model such as compressional wave speed, V_p , and density, ρ , are
222 scaled to the isotropic shear wave speed model, V_s . V_p is converted from V_s using a V_p
223 to V_s ratio such that V_p/V_s is 2.0 in the sediments and 1.75 in the crystalline crust and
224 mantle, consistent with a Poisson solid. For density, we use a scaling relation that has

225 been influenced by the studies of *Christensen and Mooney* [1995] and *Brocher* [2005] in
226 the crust, and by *Karato* [1993] in the mantle where sensitivity to density structure is
227 much weaker than in the crust. The Q model comes from ak135 [*Kennett et al.*, 1995]
228 with some modifications: shear Q is 600 in the upper 20 km and 400 between 20 and 80
229 km depth outside the Tibetan Plateau, while we set it to 250 within the Tibetan Plateau
230 [*Levshin et al.*, 2010]. V_s , V_{sv} , and V_{sh} are converted to a reference period of 1 sec. To
231 test the effect of uncertainties in the physical dispersion correction [*Kanamori and*
232 *Anderson*, 1977] on estimates of V_{sv} and V_{sh} caused by ignorance of the Q of the crust,
233 we tested by lowering values of Q from 250 to 100 between 20 and 80 km depth. We
234 found that the amplitude of the resulting depth averaged crustal radial anisotropy only
235 decreased from 3.14% to 3.13% for the smaller Q beneath point B shown in Figure 1a.
236 As a constant Q of 100 between these depths is almost certainly too low, and we are
237 concerned with anisotropy greater than 1%, uncertainties in the Q model can be ignored
238 here.

239 To avoid consideration of physically unreasonable models, we imposed prior constraints
240 on the parameter space explored in the inversion. (1) Although velocity is not constrained
241 to increase monotonically with depth, it cannot decrease with depth at a rate ($-\Delta v/\Delta h$)
242 larger than $1/70 \text{ s}^{-1}$. This constraint reduces (but does not eliminate) the tendency of the
243 shear-wave speeds to oscillate with depth. (2) Shear-wave speeds increase with depth
244 across the sediment-basement interface and across Moho. (3) Both V_{sv} and V_{sh} are
245 constrained to be less 4.9 km/s at all depths. (4) The amplitude of radial anisotropy in the
246 uppermost and lowermost crust is constrained by setting $V_{sh}=V_{sv}$ for splines 1 and 5

247 (Figure 5). The last constraint is imposed to mitigate against radial anisotropy oscillating
248 with depth, and its effect is discussed further in Section 5.4.1.

249 The model space is then explored starting with perturbations (Table 1) to a reference
250 model consisting of sedimentary structure from CRUST 2.0 [Bassin *et al.*, 2000] and
251 crystalline crustal and uppermost mantle structure from *Shapiro and Ritzwoller* [2002].
252 Imposing the prior constraints in model space defines the prior distribution of models
253 (white histograms in Figure 6), which aims to quantify the state of knowledge before data
254 are introduced.

255 **3.2 Inversion procedure**

256 With the parameterization and constraints described above, we perform the Bayesian
257 Monte Carlo inversion based on the method described by *Shen et al.* [2013b]. This
258 method is modified to produce a radially anisotropic model using both Love and
259 Rayleigh wave data without receiver functions. The main modifications lie in the forward
260 calculation of surface wave dispersion for a transversely isotropic (radially anisotropic)
261 medium, which we base on the code MINEOS [*Masters et al.*, 2007]. Unlike most
262 seismic dispersion codes, the MINEOS code models a transversely isotropic medium. In
263 order to accelerate the forward calculation, we compute numerical first-order partial
264 derivatives relative to each model parameter. Given the range of model space explored,
265 the use of first-derivatives is sufficiently accurate [*James and Ritzwoller*, 1999; *Shapiro*
266 *and Ritzwoller*, 2002]. For every spatial location, we start from the reference model
267 described above, \mathbf{p}_{ref} , and the corresponding Rayleigh or Love wave dispersion curves,
268 \mathbf{D}_{ref} , and the partial derivatives ($\partial D / \partial p_i$) are computed for all 16 free parameters using

269 the MINEOS code. With these partial derivatives, dispersion curves \mathbf{D} for any model \mathbf{p}
 270 may be approximated as:

$$271 \quad \mathbf{D} = \mathbf{D}_{ref} + \sum_i \left(\frac{\partial \mathbf{D}_{ref}}{\partial p_i} \right) \delta p_i \quad (1)$$

272 where $\delta p_i = p_i - p_{ref\ i}$, is the perturbation to model parameter i .

273 The model space sampling process is guided by the Metropolis law, and goes as follows.

274 Within the model space defined by the prior information, an initial model m_0 is chosen
 275 randomly from the prior distribution, and its likelihood function $L(m_0)$ is computed:

$$276 \quad L(m) = \exp \left(-\frac{1}{2} S(m) \right) \quad (2)$$

277 where

$$278 \quad S(m) = S_{Rayleigh} + S_{Love} = \sum_i \frac{(D(m)_i^{pred} - D_i^{obs})^2}{\sigma_i^2} + \sum_i \frac{(D'(m)_i^{pred} - D'_i^{obs})^2}{\sigma_i'^2} \quad (3)$$

279 where $D(m)_i^{pred}$ is the predicted phase velocity for model m at period i (computed from
 280 (1)), and D_i^{obs} is the observed phase velocity. Here, D represents Rayleigh wave phase
 281 velocities and D' indicates Love wave phase velocities. Standard deviations of the
 282 Rayleigh and Love wave phase velocity measurements are given by σ and σ' ,
 283 respectively.

284 A new model m_i is generated by perturbing the initial model m_0 following the procedure
 285 described by *Shen et al.* [2013b], and its likelihood function $L(m_i)$ is obtained through a
 286 similar computation as described above. The model m_i is accepted or rejected according
 287 to a probability function P defined as follows:

$$288 \quad P_{accept} = \min (1, L(m_i)/L(m_0)) \quad (4)$$

289 If m_i is accepted, the next model sampled in model space will be based on it rather than
 290 m_0 . If m_i is not accepted, sampling continues until the likelihood function levels off. After
 291 the likelihood function levels off a new initial models is chosen randomly from the prior
 292 distribution. The process is continued until at least 5000 models have been accepted from
 293 at least 5 initial starting points. We then calculate average values of each parameter in
 294 the >5000 accepted models and take that average as a new reference model, and then
 295 recalculate dispersion curves and partial derivatives. With this new reference model and a
 296 similar sampling procedure, we repeat the process until we find an additional 5000
 297 models accepted from at least 10 initial starting points. The use of various initial models
 298 minimizes the dependence on the initial parameters, but we find that initial model
 299 dependence is weak. That is, convergence tends to be to similar models irrespective of
 300 the initial model starting point. When the algorithm terminates at each location, the
 301 Rayleigh and Love wave phase velocity curves are recomputed for each accepted model
 302 using MINEOS rather than the partial derivatives.

303 The Monte Carlo sampling will generate an ensemble of anisotropic models that fit the
 304 data better than the reference model. The ensemble is reduced further in size by an
 305 additional acceptance criterion defined as follows:

$$\chi \leq \begin{cases} \chi_{min} + 0.5 & \text{if } \chi_{min} < 0.5 \\ 2 \chi_{min} & \text{if } \chi_{min} \geq 0.5 \end{cases}$$

306 where misfit $\chi = \sqrt{S/N}$ is the square root of reduced chi-squared value, S is defined by
 307 equation (3), and N is the number of observed data (number of discrete points along the
 308 Rayleigh and Love wave phase velocity curves). Thus, on average, this posterior
 309 distribution includes models whose misfit is less than about twice that of the best-fitting
 310 model, which has a square root of reduced chi-squared value of χ_{min} .

311 Finally, the mean and standard deviation of V_{sv} and V_{sh} are used to summarize the
312 posterior distribution for each depth and location. As an example, consider point B
313 (Figure 1a), where mid-crustal anisotropy is needed to fit the data (Figure 6). The widths
314 of the posterior distributions reflect how well V_{sv} , V_{sh} , and their differences are
315 constrained at each depth. Uncertainties in shear wave speeds at depths of 20 and 35 km
316 are ~ 0.1 km/s, but ~ 0.2 km/s at 50 km. Moreover, radial anisotropy is inescapable at 20
317 and 35 km, but not required, if still likely, at 50 km. The poorer resolution at 50 km
318 results from the lack of long-period Love wave data, increasing data uncertainties with
319 period, and the tradeoff between lower crustal and uppermost mantle structures.
320 Therefore, as mentioned earlier, we mainly focus discussion on structures no deeper than
321 about 50 km.

322 We performed the Bayesian Monte Carlo inversion at every grid point in the study region
323 to produce posterior distributions. In Section 4, we present and interpret spatial variations
324 in the means and standard deviations of the distribution. Then in Section 5, we query the
325 entire distribution to address particular scientific questions.

326 **4. Inversion Results**

327 **4.1 Example results at various locations**

328 As examples of local dispersion curves and the results of their inversion to produce a
329 radially anisotropic model, we consider results at four locations in different parts of
330 eastern Tibet and its surroundings (Figure 1a, points A-D). For point A, which is north of
331 the Kunlun fault, near the eastern edge of the Qaidam Basin, the gray-shaded areas of the
332 inverted model representing the 1σ uncertainty of the posterior distribution of accepted
333 models in V_{sh} and V_{sv} (Figure 7b) give no indication of radial anisotropy. V_{sh} and V_{sv}

334 are approximately equal in the crust, and no Rayleigh-Love discrepancy is observed. In
335 contrast, for point B in in the middle of eastern Tibet, large differences are required in
336 V_{sh} and V_{sv} between ~ 20 and 50 km depth, as large as about $7.8\% \pm 1.6\%$ (Figure 7d).
337 The model uncertainty increases near the base of the sedimentary layer (not shown) and
338 near the Moho, which reflects the velocity-depth tradeoff near interfaces characteristic of
339 surface wave inversions. This prevents precise imaging of the discontinuities using
340 surface waves alone. Although the inversion is performed to a depth of 200 km, we
341 concentrate discussion on the crust where radial anisotropy is well resolved.

342 For point C in the Sichuan Basin, the Rayleigh and Love wave dispersion curves call for
343 anisotropy only in the upper 20 km of crust (Figure 7f). As discussed in Section 4.3, the
344 anisotropy could be confined to the sediments but would need to be about four times
345 stronger. For point D in the Longmenshan region, mid-crustal radial anisotropy is
346 required, but in this case, $V_{sv} > V_{sh}$, and radial anisotropy is negative.

347 In Figure 7, green lines on the dispersion curves represent the predicted curves for the
348 isotropic V_s model in the crust, although the mantle contains radial anisotropy. They
349 show how the isotropic model misfits the data at points B, C, and D where radial
350 anisotropy is required in the middle crust.

351 **4.2 Maps of V_{sv} , V_{sh} , and Voigt-averaged V_s**

352 Maps of the mean of the resulting posterior distributions for V_{sv} , V_{sh} , and the Voigt
353 averaged isotropic V_s in the middle crust of Tibet (~ 35 km) are shown in Figure 8, in
354 addition to the mean of crustal thickness. The most prominent feature is the low mid-
355 crustal shear wave speed across all of eastern Tibet compared with much higher speeds
356 outside of Tibet. In the mid-crustal V_{sv} map (Figure 8a), anomalies are similar to those

357 presented in an earlier study using a similar data set [Yang *et al.*, 2012]. The Vsh model is
358 faster than Vsv across the high plateau, indicating strong positive radial anisotropy.
359 Combining Vsv and Vsh, an isotropic Vs estimate is computed from the Voigt averaging
360 method mentioned in Section 1. In these maps, white contours outline regions with shear
361 wave speeds lower than 3.4 km/s, below which partial melting may be expected to exist
362 [Yang *et al.*, 2012]. Although $V_{sv} < 3.4$ km/s exists across much of eastern Tibet, $V_{sh} >$
363 3.4 km/s is present across the majority of the region. The difference between Vsv and
364 Vsh causes the white contour in the Vsv map to contract toward the interior of eastern
365 Tibet in the Vs map, predominantly within the Songpan-Ganzi and the northern
366 Chuandian terrane. This feature of the Vs model is discussed further in Section 5.

367 **4.3 Radial anisotropy**

368 From the posterior distributions of Vsv and Vsh at each location we obtain the radial
369 anisotropy model. Radial anisotropy at different depths and along different vertical
370 profiles is shown in Figures 9 and 10. In this section we first discuss the distribution of
371 radial anisotropy qualitatively, and then the estimated uncertainties are presented and
372 discussed in Section 4.4.

373 In the upper crust (Figure 9a), radial anisotropy beneath the Tibetan Plateau is negative,
374 on average. Beneath the Sichuan Basin, in contrast, it is positive with amplitudes in
375 excess of 6%. Actually, the depth extent of the strong upper crustal radial anisotropy
376 beneath the Sichuan Basin is not well constrained by the data. For example, it could also
377 be confined to the sediments, but in this case radial anisotropy of about 25% would be
378 needed to fit the data. Because of this exceptionally large amplitude, we prefer a model
379 with radial anisotropy confined to the upper crystalline crust.

380 In the middle crust (Figure 9b), relatively strong positive radial anisotropy with
381 amplitudes ranging from 4% to 8% is observed across most of eastern Tibet, where the
382 strongest anisotropy is concentrated near the northern margin of the Qiangtang terrane.
383 Near the northern and eastern margins of the Tibetan Plateau, radial anisotropy decreases
384 in amplitude. To the north, radial anisotropy decreases abruptly across the Kunlun fault,
385 and to the east radial anisotropy decreases and becomes negative near the Longmenshan
386 west of the Sichuan Basin. The northern margin of radial anisotropy closely follows the
387 Kunlun fault. In contrast, the termination of radial anisotropy near the southeastern
388 margin of Tibet does not follow the topography or geological boundaries. Strong radial
389 anisotropy covers only the northern half of the Chuandian terrane and it ends before the
390 plateau drops off and topography decreases. To the east of the Tibetan Plateau, negative
391 radial anisotropy shows up near the Longmenshan, in a narrow strip between the
392 Chuandian terrane and the Sichuan Basin. Outside the Tibetan Plateau, mid-crustal radial
393 anisotropy is weak except within and south of the Sichuan Basin and in the Qilian
394 terrane.

395 In the lower crust (Figure 9c), radial anisotropy is weak across most of the region of
396 study, with notable isolated anomalies in the northern Songpan-Ganzi and Qiangtang
397 terranes. In fact, radial anisotropy at this depth cannot be reliably determined as
398 anisotropy trades off with both Moho depth and radial anisotropy in the uppermost
399 mantle. This phenomenon is reflected in the large uncertainties shown in Figure 10c.

400 In Figure 9d, uppermost mantle anisotropy at 85 km depth is shown, which is taken from
401 the model of *Shapiro and Ritzwoller* [2002], as mentioned in Section 3.1. Shapiro's
402 model of anisotropy is fairly uniform across the study region with an average positive

403 anisotropy of ~6%, but much weaker anisotropy exists at this depth within and south of
404 the Sichuan Basin. In fact, weak negative anisotropy exists beneath parts of the Sichuan
405 Basin in their model.

406 The locations of four vertical transects are shown in Figure 9a and the vertical transects
407 themselves are presented in Figure 10. For profile A, V_{sv} , V_{sh} , and radial anisotropy are
408 presented. For profiles B, C, and D, only radial anisotropy is presented.

409 For profile A, V_{sv} is similar to the result presented by *Yang et al.* [2012] using a similar
410 data set. Within the high plateau, a V_{sv} minimum in the middle crust is seen clearly from
411 about 20 to 40 km depth. In the Sichuan Basin, a very slow sedimentary layer is present
412 along with faster lower crust. Compared to V_{sv} , V_{sh} is faster from the surface to the base
413 of the crust except in the uppermost crust of the high plateau. V_{sh} in the middle crust of
414 the high plateau is so fast that the velocity minimum seen for V_{sv} is much more subtle.
415 There are differences in upper crustal V_{sv} and V_{sh} in the Sichuan Basin as well. Radial
416 anisotropy beneath the high plateau along profile A increases from an average of about -
417 1% in the uppermost crust to values of 4% to 6% between 30 and 40 km depth. Radial
418 anisotropy then decreases with depth in the lower crust. Near the eastern edge of the
419 plateau, radial anisotropy vanishes as surface elevation falls off, perhaps changing sign
420 before elevation plummets at the Longmenshan.

421 The three other vertical profiles shown in Figure 10 are similar to profile A in the vertical
422 distribution of radial anisotropy in the crust across the Tibetan Plateau: radial anisotropy
423 is negative, on average, in the uppermost crust, positive and peaks in amplitude in the
424 middle crust, decreases in the lower crust, and terminates horizontally near the border of
425 the high plateau except within and south of the Sichuan Basin. The nature of the

426 termination of radial anisotropy near the border of the plateau varies from place to place.
427 For example, in profile C, which runs across the northeastern part of the plateau, radial
428 anisotropy decreases gradually as topography decreases. In contrast, in profile D, which
429 goes through the southeastern part of the plateau, radial anisotropy ends abruptly before
430 topography decreases.

431 In summary, within the Tibetan Plateau, strong positive radial anisotropy begins at about
432 20 km depth and peaks between 30 and 40 km depth. It is almost continuous between
433 different terranes, but there is some diminishment in amplitude near terrane boundaries as
434 profile B illustrates. Radial anisotropy has a somewhat broader depth range in the
435 Qiangtang terrane compared with other terranes. Outside of the Tibetan plateau, strong
436 upper-to-middle crustal radial anisotropy shows up in and south of the Sichuan Basin.
437 Negative anisotropy is mostly confined to the uppermost crust beneath Tibet and in the
438 middle crust in the Longmenshan region, near the border between Tibet and the Sichuan
439 Basin.

440 **4.4 Uncertainty in radial anisotropy**

441 Figure 11 presents uncertainties in the estimated radial anisotropy in the region of study
442 at depths of 10 and 35 km, as well as at a depth located at 90% of crustal thickness. The
443 uncertainty is defined as the one standard deviation of the posterior distribution at each
444 depth. Except beneath the Sichuan Basin, uncertainties grow with depth in the crust
445 because a smaller percentage of the observed dispersion curves are sensitive to the
446 greater depths. Beneath the Sichuan Basin, the higher shallow uncertainties result from
447 the trade-off of shear velocities in the crystalline crust and sediments. At 10 km depth,
448 the average uncertainty in eastern Tibet is about 1%, whereas in the mid-crust it is about

449 2%, and in the lower crust it is about 3.5%. As discussed in Section 5.4.1, if we had not
450 constrained $V_{sh}=V_{sv}$ for crustal B-splines 1 and 5 (Figure 5) in the uppermost and
451 lowermost crust, uncertainties in radial anisotropy in the uppermost and lowermost crust
452 would have been larger. Still, the higher uncertainty in the lower crust is why we
453 concentrate discussion on shallower depths. The higher uncertainties in the lower crust
454 result from the fact that Love waves do not constrain V_{sh} well at these depths and there
455 are trade-offs with crustal thickness and uppermost mantle structure.

456 **4.5 Computation of regional averages**

457 Several of the attributes of the model observed here appear to be fairly homogeneous
458 over extended areas. These attributes include positive mid-crustal radial anisotropy
459 beneath eastern Tibet and the Sichuan Basin, negative mid-crustal radial anisotropy near
460 the Longmenshan adjacent to the eastern border of Tibet, negative radial anisotropy in the
461 shallow crust beneath parts of eastern Tibet (notably the Songpan-Ganzi terrane), and V_s
462 in the mid-crust beneath eastern Tibet. We present here averages of the means and the
463 standard deviations of the mean of these variables defined over the four regions. These
464 standard deviations, in contrast with those presented in Figure 11 and discussed in
465 Section 4.4, principally reflect spatial variations rather than uncertainties.

466 There are four regions over which we compute the averages. First, we consider “eastern
467 Tibet” to be defined by the interior of the 84.2% probability contour (orange, red colors)
468 of positive mid-crustal radial anisotropy near Tibet, which is presented later in the paper
469 (Figure 13a). This contour approximately follows the outline of the high plateau. Second,
470 we consider the Longmenshan region near the border between Tibet and the Sichuan
471 Basin to be contained within the 15.8% probability contour (blue colors) of positive mid-

472 crustal radial anisotropy (Figure 13a). Finally, we use the geological outlines of the
473 Sichuan Basin and the Songpan-Ganzi terrane as the third and fourth regions.

474 In the Songpan-Ganzi terrane, the distribution of the means of shallow crustal (~10 km)
475 radial anisotropy is presented in Figure 12a. The average of the means in this region is -
476 $1.03\% \pm 1.38\%$. This is the structural attribute with the relatively largest variability. The
477 distribution of the means of mid-crustal radial anisotropy across eastern Tibet (~35 km)
478 and the Sichuan Basin (~15 km) are presented in Figures 12b,c. Mid-crustal radial
479 anisotropy averages $4.81\% \pm 1.41\%$ in eastern Tibet. Across the Sichuan Basin the
480 average is somewhat larger, $5.35\% \pm 1.43\%$. Also in the middle crust, but averaged over
481 the Longmenshan region (~30 km), the distribution of the means of mid-crustal radial
482 anisotropy is presented in Figure 12d. The average is $-2.80\% \pm 0.94\%$. Finally, mid-
483 crustal Vs averaged over eastern Tibet is $3.427 \text{ km/s} \pm 0.050 \text{ km/s}$, as seen in Figure 12e.

484

485

486 **5. Identifying highly probable model attributes**

487 The means of the posterior distributions of the models that result from the Bayesian
488 Monte Carlo inversion of Rayleigh and Love wave dispersion curves have been used to
489 infer that (1) positive ($V_{sh} > V_{sv}$) mid-crustal radial anisotropy exists across the entirety
490 of eastern Tibet with an average amplitude of about 4.8% (~35 km) and at much
491 shallower depths (~15 km) beneath the Sichuan Basin with an average amplitude of about
492 5.4%, (2) weaker negative radial anisotropy ($V_{sh} < V_{sv}$) appears in the middle crust (~30
493 km) along the Longmenshan region (-2.8%) and in the shallow crust (~10 km) across the

494 Songpan-Ganzi terrane (-1.03%) , and (3) the Voigt averaged shear wave speed in the
495 middle crust (~35 km) averages about 3.427 km/s across eastern Tibet. From the
496 geographical spread of the local means of the posterior distributions of these attributes we
497 have inferred that these observations are characteristic of each region. Radial anisotropy
498 in the lowermost crust is more poorly constrained than at shallower depths because of a
499 trade-off with crustal thickness and radial anisotropy in the mantle.

500 Although the mean of the posterior distribution is interpreted as its maximum likelihood,
501 the Bayesian Monte Carlo inversion delivers a distribution of models at each depth. For
502 this reason, within a Bayesian framework, the probability that the model achieves
503 particular attributes can be computed. Here we address the following questions across the
504 region of study: (1) What is the probability that positive ($V_{sh} > V_{sv}$) radial anisotropy
505 exists in the shallow crust or in the middle crust? (2) Similarly, what is the probability for
506 negative radial anisotropy? (3) What is the probability that the Voigt averaged shear
507 wave speed lies below or above 3.4 km/s in the middle crust?

508 In computing these probabilities, we acknowledge that the posterior distribution
509 represents a conditional probability in which the likelihood is conditioned on prior
510 information that appears in the range of the model variables allowed, the constraints
511 imposed, the parameterization chosen, the details of the search algorithm, and the
512 assumptions made (e.g., ρ/V_s , V_p/V_s , Q). From a Bayesian perspective, the distribution
513 represents the authors' degree of belief in the results, but if the prior information is wrong
514 then the resulting distribution of models may be biased. We identify several potential
515 sources for bias, including crustal thickness and uppermost mantle radial anisotropy in

516 the reference model and the fixed crustal V_p/V_s ratio, and discuss how these choices may
517 affect the mean of the estimated posterior distribution of the selected model attributes.

518 **5.1 Computing the probability of a model attribute from the posterior distribution**

519 Figure 13a,b illustrates the computation of the probability for the existence of positive
520 radial anisotropy in the middle crust. The probability that $V_{sh} > V_{sv}$ (positive radial
521 anisotropy) at 35 km depth is mapped in Figure 13a. It is computed at each point from the
522 local posterior distribution, examples of which are shown for locations A, B, and D from
523 Figure 1a in Figure 13b. For point A, a location that we interpret as isotropic in the crust,
524 approximately half (54%) of the posterior distribution shows positive anisotropy and half
525 negative. For point B, which we interpret as possessing strong positive mid-crustal
526 anisotropy, 100% of the posterior distribution has $V_{sh} > V_{sv}$ at 35 km depth. For point D,
527 where we observe negative anisotropy on average, only $\sim 0.12\%$ of the models in the
528 posterior distribution have $V_{sh} > V_{sv}$. Thus, at this point, more than 99.8% of the models
529 in the posterior distribution display negative anisotropy in the middle crust.

530 The values mapped in Figure 13a are simply the percentage of models in the posterior
531 distribution at each point with positive mid-crustal radial anisotropy. Examples of the
532 probability of positive radial anisotropy at depths of 10 and 15 km are also shown in
533 Figure 13c,d. Similarly, from the local posterior distributions of the isotropic V_s , the
534 probabilities that V_s is greater than 3.4 km/s or less than 3.4 km/s are mapped in Figure
535 14.

536 In general, we consider a model attribute (e.g., $V_{sh} > V_{sv}$, $V_s < 3.4$ km/s) to be “highly
537 probable” if it appears in more than 97.8% of the models in the posterior distribution. In
538 this case, all or nearly all of the models in the posterior distribution possess the specified

539 attribute. If the attribute appears in less than 2.2% of the accepted models, then the
540 converse of the attribute (e.g., $V_{sh} < V_{sv}$, $V_s > 3.4$ km/s) would be deemed “highly
541 probable”. One could introduce other grades of probability (e.g., probable, improbable,
542 the converse is probable, etc.), but we do not do so here.

543 **5.2 Regions with high probability of positive or negative radial anisotropy**

544 High probability regions for positive radial anisotropy in the middle crust appear as red
545 colors in Figure 13a and for negative mid-crustal anisotropy as dark blue regions. Red
546 colors cover most of eastern Tibet, including the Qiangtang terrane, most of the Songpan-
547 Ganzi terrane, and the northern Chuandian terrane. Another region strongly favoring
548 positive mid-crustal radial anisotropy lies south of the Sichuan Basin, largely in Yunnan
549 province. Mid-crustal radial anisotropy has a lower average probability there (orange
550 colors, Figure 13a) than beneath Tibet, because the crust is thinner (~40 km) and at 35
551 km depth crustal radial anisotropy trades-off with crustal thickness and uppermost mantle
552 radial anisotropy. Blue colors appear in the Longmenshan region near the border of Tibet
553 and the Sichuan Basin, indicating the high probability of negative mid-crustal radial
554 anisotropy there.

555 At shallower depths, the high probability zones of positive or negative radial anisotropy
556 are smaller and more variable than in the middle crust. At 10 km depth (Figure 13c),
557 highly probable negative radial anisotropy is mainly confined to the Songpan-Ganzi
558 terrane but also extends into parts of the Qiangtang and Chuandian terranes. By 15 km
559 (Figure 13d), neither positive nor negative radial anisotropy attains high probabilities
560 pervasively across Tibet, but positive radial anisotropy is highly probable across most of
561 the Sichuan Basin.

562 **5.3 Probability of low shear wave speeds in the middle crust**

563 Middle-to-lower crustal low velocity zones (LVZ) have been reported in several studies
564 [*Yao et al.*, 2008; *Yang et al.*, 2012], but most of these considered V_{sv} alone. The
565 existence of crustal radial anisotropy with $V_{sh} > V_{sv}$ across most of eastern Tibet
566 increases the Voigt-averaged shear wave speed relative to V_{sv} , and reduces the strength
567 of a crustal LVZ. *Yang et al.* [2012] argued that 3.4 km/s is the speed below which partial
568 melt may plausibly begin to occur at a depth of about 35 km depth, although this
569 threshold is poorly known and is probably spatially variable. At this depth, the mean
570 value of the Voigt average shear wave speed in the posterior distribution is shown in
571 Figure 8c and the distribution of the mean values across eastern Tibet is presented in
572 Figure 12e. Although shear wave speeds across eastern Tibet average 3.427 km/s, there is
573 substantial spatial variability and the likelihood that V_s dips below 3.4 km/s in some
574 locations is high.

575 In the attempt to quantify the likelihood of shear wave speeds less than 3.4 km/s in the
576 middle crust, Figure 14 presents the percentage of models in the posterior distribution at
577 each point with $V_s > 3.4$ km/s and $V_s < 3.4$ km/s at 35 km depth. As Figure 14a shows,
578 $V_s > 3.4$ km/s is highly probable across most of the study region, but does not rise to the
579 level of high probability across much of Tibet. Conversely, Figure 14b shows that $V_s <$
580 3.4 km/s at this depth is also not highly probable across most of the high plateau.

581 Unfortunately, this means that we cannot infer with high confidence either that mid-
582 crustal V_s is greater than or less than 3.4 km/s across much of Tibet. However, there are
583 two disconnected regions where more than 97.8% of the accepted model have $V_s < 3.4$
584 km/s, such that we would infer the high probability of $V_s < 3.4$ km/s. These regions are

585 in the northern Songpan-Ganzi terrane near the Kunlun fault and in the northern
586 Chuandian terrane. A third region of low V_s that nearly rises to the level of high
587 probability lies in the northern Qiangtang terrane.

588 **5.4 Caveats: Quantifying the potential for bias in the posterior distribution**

589 Measurements of mid-crustal radial anisotropy, particularly its amplitude, and of shear
590 wave speed V_s , particularly the minimum value it attains in the middle crust, are affected
591 by a variety of information introduced in the inversion, including the parameterization of
592 crustal radial anisotropy, crustal thickness in the reference model, the fixed amplitude of
593 radial anisotropy in the mantle, and the fixed value of the V_p/V_s ratio in the crust. Errors
594 in these variables can bias the posterior distribution and introduce a systematic error that
595 could render the probability estimates presented in Sections 5.1 to 5.3 biased.

596 In the following we discuss the effects of constraints on radial anisotropy in the crust,
597 crustal thickness and the fixed amplitude of upper mantle radial anisotropy in the input
598 reference model, and uncertainties in the fixed crustal V_p/V_s ratio.

599 **5.4.1 Relaxing constraints on radial anisotropy in the uppermost and lowermost** 600 **crust**

601 All results presented above include the constraint that $V_{sh}=V_{sv}$ for the crustal B-splines
602 1 and 5 (Figure 5). Figure 15 shows the range of the means of the posterior distributions
603 for radial anisotropy averaged across the high plateau with this constraint applied (blue
604 bars). This is compared with a similar spatial average computed without the constraint
605 (red bars), so that the number of unknowns increases from 16 to 18. The less constrained
606 inversion approximately encompasses the more tightly constrained result. The relaxation

607 of the constraint on radial anisotropy increases the variability of the model, particularly in
608 the uppermost and lowermost crust and shifts the mean of the distribution in the
609 lowermost crust to larger values. Between depths of 25 and 45 km, however, the means
610 of the distributions are nearly indistinguishable, implying that this constraint does not
611 bias estimates of mid-crustal radial anisotropy.

612 **5.4.2 Crustal thickness and mantle radial anisotropy**

613 The crustal thickness in the reference model (around which the Monte Carlo search
614 occurs) and the fixed amplitude of radial anisotropy in the mantle do affect aspects of the
615 posterior distribution in the middle crust, including the amplitude of radial anisotropy and
616 the isotropic shear wave speed. The effects of these properties of the deeper parts of the
617 model will be stronger, however, where the crust is thinner. This is reflected in the
618 uncertainties in mid-crustal radial anisotropy shown in Figure 11. Uncertainties are
619 smaller across eastern Tibet ($\sim 1.75\%$) where the crust is thicker than in adjacent regions
620 ($2.0\text{-}3.0\%$). Indeed, we find that changes in crustal thickness in the reference model and
621 in the fixed amplitude of radial anisotropy in the mantle do not strongly and
622 systematically affect either the amplitude of radial anisotropy or isotropic V_s in the
623 middle crust beneath eastern Tibet. However, these changes do have a systematic impact
624 on these model attributes where the crust is thinner, for example in the Longmenshan
625 region near the border of Tibet and the Sichuan Basin. For this reason, we present results
626 here of the impact of changing crustal thickness in the reference model and the amplitude
627 of mantle radial anisotropy at location D (Figure 1a) in the Longmenshan region.

628 Figure 16a,b presents the estimates of depth averaged (± 5 km around the middle crust)
629 mid-crustal radial anisotropy as well as depth averaged mid-crustal V_s , which result by

630 changing the fixed amplitude of mantle radial anisotropy averaged from Moho to 150 km
631 depth. Errors bars reflect the one standard deviation variation in the posterior distribution
632 in each of the inversions, which are done identically to the inversions used to produce the
633 model described earlier in the paper (which is the middle error bar with a triangle in the
634 center on each panel of Figure 16a,b). The effect of mantle radial anisotropy on Vs is
635 very weak but increasing mantle radial anisotropy does systematically change crustal
636 radial anisotropy. Changing the depth-averaged mantle radial anisotropy from about 4%
637 to 0% or 10% changes the estimated depth-averaged crustal radial anisotropy by less than
638 $\pm 1\%$. Because we believe that mantle radial anisotropy is probably known better than this
639 range, this possible systematic shift in crustal radial anisotropy is probably an
640 overestimate. Still, it lies within the stated errors of crustal radial anisotropy in the
641 Longmenshan region. If potential systematic errors lie within stated uncertainties, we
642 consider them not to be the cause for concern.

643 Similarly, Figure 16c,d presents estimates of depth averaged (± 5 km around the middle
644 crust) mid-crustal radial anisotropy and depth averaged mid-crustal Vs caused by
645 changing crustal thickness in the reference model. Again, the middle error bar is the
646 result of the inversion for the model presented earlier in this paper, so that in the
647 Longmenshan region the crustal thickness of the reference model was about 50 km.
648 Changing the crustal thickness in the reference model (around which the Monte Carlo
649 inversion searches) from 40 to 60 km has a systematic affect both on crustal radial
650 anisotropy and mid-crustal isotropic Vs. But, again, the effect is relatively small ($\pm 0.5\%$
651 in mid-crustal radial anisotropy, ± 25 m/s in mid-crustal Vs). Although the range of
652 crustal thickness considered is considerably larger than what we consider physically

653 plausible for this location, the effect on model characteristics is below the stated model
654 uncertainty.

655 Therefore, both mid-crustal Vs and the mid-crustal radial anisotropy are affected by the
656 fixed amplitude of mantle radial anisotropy and the crustal thickness in the reference
657 model, but the effects are below estimated model uncertainties and could only become
658 significant if the effects were correlated and would add constructively. Although this is
659 possible, in principle, it is unlikely to occur systematically across the region. Tighter
660 constraints on crustal thickness and mantle radial anisotropy would result from the joint
661 interpretation of receiver functions and longer period dispersion measurements from
662 earthquakes. Uncertainties in these quantities, therefore, are expected to reduce over time,
663 but we believe that these improvements will not change the results presented here
664 appreciably.

665 **5.4.3 Vp/Vs in the crust**

666 The strongest and also the most troubling of the remaining parameters that may produce a
667 systematic error in estimates of radial anisotropy is crustal Vp/Vs, which has been fixed
668 in the crust at $Vp/Vs = 1.75$, the value for a Poisson solid which is generally considered
669 to be typical of continental crust [*Zandt and Ammon, 1995; Christensen, 1996*]. Although
670 normal Vp/Vs (~ 1.75) has been widely observed across much of eastern Tibet [*Vergne et*
671 *al., 2002; Xu et al., 2007; Wang et al., 2010; Mechie et al., 2011, 2012; Yue et al., 2012*],
672 very low crustal Vp/Vs values also have been observed in the northern Songpan-Ganzi
673 terrane [*Jiang et al., 2006*], and very high crustal Vp/Vs has been observed near the
674 Kunlun fault [*Vergne et al., 2002*], the eastern margin of the plateau [*Xu et al., 2007*];

675 *Wang et al.*, 2010], as well as parts of the Qiangtang terrane [*Yue et al.*, 2012]. Thus, the
676 assumption of a uniform V_p/V_s across all of Tibet may be inappropriate.

677 To test the effect of the assumption that crustal $V_p/V_s=1.75$ on the amplitude of mid-
678 crustal radial anisotropy, we have inverted with different crustal V_p/V_s ratios and have
679 plotted the resulting depth-averaged mid-crustal radial anisotropies for point B (Figure 1a)
680 in Figure 17a. We apply these tests at a point in eastern Tibet, in contrast with the tests
681 presented in Section 5.4.2, which were for the Longmenshan region. Positive correlation
682 is observed between the applied crustal V_p/V_s and depth-averaged radial anisotropy, and
683 mid-crustal radial anisotropy may become zero when V_p/V_s drops below 1.60. This
684 extremely low V_p/V_s could exist in regions where the Alpha-Beta quartz transition
685 (ABQT) occurs, namely in a thin layer that occurs somewhere between 20 to 30 km depth
686 [*Mechie et al.*, 2011]. Also, a relatively low crustal V_p/V_s may be caused by crust with a
687 felsic composition [*Mechie et al.*, 2011]. However, both alternatives are for a thin low
688 V_p/V_s layer, not the whole crust, and it is physically unlikely to have an average crustal
689 V_p/V_s of 1.60. With values of V_p/V_s ranging from 1.70 to 1.80, the affect is to change
690 the amplitude of radial anisotropy only by about $\pm 1\%$. Although radial anisotropy is
691 required across eastern Tibet, the reliability of estimates of its amplitude would be
692 improved with better information about V_p/V_s across Tibet.

693 The value of crustal V_p/V_s not only affects the amplitude of crustal radial anisotropy, but
694 also the shear wave speed (V_s). Figure 17b shows that crustal V_p/V_s and depth averaged
695 mid-crustal V_s are anti-correlated, with V_s decreasing as crustal V_p/V_s increases. This
696 result may seem counterintuitive. With a fixed V_p/V_s , increasing radial anisotropy will
697 increase V_s . In addition, increasing V_p/V_s tends to increase radial anisotropy.

698 Nevertheless, increasing V_p/V_s reduces V_s because increasing V_p at a constant V_s
699 increases the Rayleigh wave speed but not the Love wave speed. In this case, V_{sv} must
700 be lowered to reduce the Rayleigh wave speed in order to fit the Rayleigh-Love
701 discrepancy. The lowering of V_{sv} (caused by increasing V_p/V_s) thus lowers V_s . For
702 V_p/V_s running between the physically more plausible range of 1.7 to 1.8, the effect on
703 mid-crustal V_s is well within stated uncertainties, about ± 9 m/s.

704 **5.4.4 Conclusions on potential bias in the posterior distributions**

705 We tested how systematic changes to prior information and constraints imposed in the
706 inversion affect the key model attributes that are interpreted in the paper; namely, the
707 amplitude of mid-crustal radial anisotropy and mid-crustal V_s . In particular, we tested the
708 effect of changing the fixed amplitude of radial anisotropy in the upper mantle, the
709 crustal thickness in the reference model, and the V_p/V_s ratio in the crust. In general, we
710 find that the mid-crustal radial anisotropy will become more positive (i.e., V_{sh} will
711 increase relative to V_{sv}) by reducing mantle radial anisotropy, increasing crustal
712 thickness, increasing crustal V_p/V_s . Similarly, isotropic shear wave speed V_s also
713 depends to a certain extent on these choices, being inclined to increase with increasing
714 crustal thickness and with decreasing V_p/V_s . The tests demonstrate, however, that the
715 inference of both positive and negative mid-crustal radial anisotropy is robust and
716 potential bias caused by physically realistic variations in prior information imposed in the
717 inversion should lie within the stated uncertainties of the key model attributes.

718 Improved constraints on crustal thickness and radial anisotropy in the mantle can be
719 achieved by introducing receiver functions and longer period surface wave dispersion

720 information from earthquake tomography, which are planned for the future. Providing
721 improved constraints on crustal V_p/V_s may prove to be more challenging, however.

722 **6. Discussion**

723 Taking into account the estimated probabilities and the likelihood of bias discussed in
724 Section 5 we now address two final questions: What is the most like cause of the radial
725 anisotropy observed beneath and bordering eastern Tibet? Is there pervasive partial melt
726 in the middle crust beneath eastern Tibet?

727 **6.1 On the cause of positive and negative radial anisotropy**

728 Four robust radially anisotropic features are observed. In the middle crust, positive radial
729 anisotropy is observed beneath essentially all of (1) eastern Tibet and (2) the Sichuan
730 Basin and (3) negative anisotropy is found beneath the Longmenshan region bordering
731 eastern Tibet and the Sichuan Basin. (4) In the upper crust, negative radial anisotropy is
732 observed beneath the Songpan-Ganzi terrane and parts of the Qiangtang and Chuandian
733 terranes. We consider the cause of the mid-crustal observations first.

734 Earlier studies [*Shapiro et al.*, 2004; *Huang et al.*, 2010] have interpreted the observation
735 of mid-crustal positive radial anisotropy beneath Tibet as evidence for the existence of
736 anisotropic crustal minerals in the middle crust. Recent experimental results, however,
737 have shown that continental crustal minerals such as quartz and feldspars act to dilute the
738 anisotropic response of mica rich rocks [*Ward et al.*, 2012]. This dilution effect may
739 raise doubt into whether crystallographic preferred orientation (CPO) of continental
740 crustal minerals alone can cause strong mid-crustal anisotropy. Open or filled fractures
741 [*Leary et al.*, 1990; *Crampin and Chastin*, 2003; *Figueiredo et al.*, 2013], grain-scale

742 effects [*Hall et al.*, 2008], sedimentary layering [*Valcke et al.*, 2006], other
743 microstructural parameters [*Wendt et al.*, 2003], and sills or lenses of partial melt
744 [*Takeuchi et al.*, 1968; *Kawakatsu et al.*, 2009] have all been discussed as mechanisms to
745 produce seismic anisotropy under certain conditions. Amongst these mechanisms, partial
746 melt may provide the most viable alternative to CPO to produce mid-crustal radial
747 anisotropy. The anisotropic effect of partial melt is less well understood and its ability to
748 produce substantial radial anisotropy is more speculative than CPO. Thus, the
749 observation of crustal radial anisotropy is still best seen as a mapping of the distribution
750 of aligned crustal minerals – albeit with the caveat that the relative fractions of mica,
751 feldspars, quartz, and amphibole remain poorly understood. In the middle crust we
752 believe that the chief contributor to strong anisotropy is a sheet silicate such as mica.
753 Even though individual mica crystals exhibit monoclinic symmetry, their tendency to
754 form sheets causes them in aggregate to approximate the much simpler hexagonal
755 symmetry [*Godfrey et al.*, 2000; *Cholach et al.*, 2005; *Cholach and Schmitt*, 2006; B.
756 Hacker, personal communication, 2012]. There is a unique symmetry axis in a hexagonal
757 system and we call the plane that is perpendicular to this axis the foliation plane. The
758 amplitude and sign of radial anisotropy reflect the orientation of the symmetry axis (or
759 foliation plane) along with the intrinsic strength of anisotropy. The amplitude of
760 azimuthal anisotropy is also affected by the orientation of the symmetry axis [*Levin and*
761 *Park*, 1997; *Frederiksen and Bostock*, 2000]. Dipping or tilted symmetry axes are
762 believed to be common in many geological settings [*Okaya and McEvilly*, 2003] and
763 should produce a combination of radial and azimuthal anisotropy.

764 Figure 18 clarifies these expectations with a synthetic calculation in which an elasticity
765 tensor with hexagonal symmetry has been rotated through a set of orientations where the
766 symmetry axis ranges from vertical ($q = 0^\circ$, transverse isotropy) to horizontal ($q = 90^\circ$),
767 similarly, the foliation plane ranges from horizontal to vertical. For a weakly anisotropic
768 medium, a transversely isotropic elasticity tensor possessing hexagonal symmetry is
769 specified by five Love parameters (A, C, F, L, and N) where $A = \rho V_{PH}^2$, $C = \rho V_{PV}^2$, $N =$
770 ρV_{SH}^2 , and $L = \rho V_{SV}^2$, ρ is density. The calculations presented here are idealized such
771 that only V_s is anisotropic ($V_{sh} \neq V_{sv}$ or $N \neq L$), there is no anisotropy in V_p ($V_{PV} =$
772 V_{PH} or $A = C$) and we set $F = A - 2L$.

773 The result of this calculation is presented in Figure 18b and yields four general
774 conclusions: Radial anisotropy (1) is positive ($V_{sh} > V_{sv}$) and its magnitude maximizes
775 for a vertical symmetry axis ($q = 0^\circ$), (2) falls to zero at an intermediate angle greater
776 than 45° ($\sim 55^\circ$ in this simulation), (3) becomes negative as the symmetry axis exceeds
777 55° , and (4) the maximum negative magnitude is less than the maximum positive
778 magnitude. Therefore, the observed amplitude of radial anisotropy is controlled by a
779 combination of the intrinsic strength of anisotropy, which results from the density of
780 anisotropic minerals and the constructive interference of their effects, and the angle that
781 the symmetry axis makes relative to the local vertical direction. The observation of
782 weaker radial anisotropy alone cannot be interpreted as evidence for a lower density of
783 anisotropic minerals. However, the observation of strong radial anisotropy is evidence for
784 the existence of anisotropic minerals aligned consistently to produce a substantial
785 anisotropic effect. In addition, positive radial anisotropy indicates that the symmetry axis
786 has a substantial vertical component (the foliation plane is largely horizontal) and

787 negative radial anisotropy implies that it has a substantial horizontal component (the
788 foliation plan is largely vertical). Because the maximum negative amplitude of radial
789 anisotropy is smaller than the maximum positive amplitude, negative anisotropy is a
790 more difficult observation. *Xie et al.* [2013] discuss these simulations and conclusions in
791 greater detail, in particular in the context of complementary observations of azimuthal
792 anisotropy. They show how the simultaneous observation of radial and azimuthal
793 anisotropy can be used to determine the orientation of the symmetry axis for a
794 hexagonally symmetric elastic tensor.

795 Based on these considerations, we conclude that the observations of positive mid-crustal
796 radial anisotropy beneath eastern Tibet and beneath the Sichuan Basin imply the
797 existence of planar mica sheets in the middle crust oriented systematically such that the
798 foliation planes are largely horizontal. As discussed by *Xie et al.* [2013], the symmetry
799 axis will not be vertical because crustal azimuthal anisotropy is observed in these regions
800 [*Yao et al.*, 2010; *Xie et al.*, 2012]. Similarly, the observation of negative mid-crustal
801 radial anisotropy along the Longmenshan region is taken as evidence for planar mica
802 sheets oriented systematically such that the foliation plane is largely vertical. By “largely
803 horizontal”, we mean that the foliation plane is probably oriented from 0° to 30° from the
804 horizontal direction. By “largely vertical”, we mean that the foliation plane is probably
805 70° to 90° degrees from the horizontal. The orientation of the foliation plane (or
806 symmetry axis) cannot be constrained accurately in the absence of information about
807 azimuthal anisotropy.

808 The orientations of the mica sheets in the middle crust probably have dynamical causes.
809 Other than to note that the micas probably orient in response to ductile deformation in the

810 middle crust, we do not speculate on the nature of the deformation that produces this
811 orientation of the mica sheets. We do note that the dip angle of faults in the
812 Longmenshan region between Tibet and the Sichuan Basin is high [*Chen and Wilson,*
813 1996], that the 2008 Wenchuan earthquake ruptured a steep fault [*Zhang et al., 2010*].
814 The change in orientation of the mid-crustal symmetry axis (or foliation plane) from
815 dominantly vertical (horizontal) in eastern Tibet to dominantly horizontal (vertical) in the
816 Longmenshan region may result from the resistance force applied by the rigid lithosphere
817 underlying the Sichuan Basin.

818 The negative anisotropy observed in the shallow crust (~10 km) across the Songpan-
819 Ganzi terrane and some other parts of eastern Tibet may also result from the CPO of
820 shallower micaceous rocks. However, earthquakes occur to a depth of about 15-20 km
821 within Tibet [*Zhang et al., 2010; Sloan et al., 2011*], so the crust near 10 km depth where
822 negative anisotropy is observed probably undergoes brittle deformation. Faults and
823 cracks in the upper crust are associated with azimuthal anisotropy [*Sherrington et al.,*
824 2004] and may also cause radial anisotropy. Negative anisotropy would result from the
825 plane of cracks or faults having a substantial vertical component. We believe this is the
826 most likely source of the observations of negative radial anisotropy in the shallow crust
827 beneath parts of eastern Tibet, particularly the Songpan-Ganzi terrane.

828 **6.2 Existence of pervasive partial melt in the middle crust beneath Tibet?**

829 Even under ideal observational circumstances in which Vs would be exceptionally well
830 constrained, it is difficult to interpret Vs in terms of the likelihood of partial melt. *Yang et*
831 *al.* [2012] present a plausibility argument for partial melt setting on below about 3.4
832 km/s. This threshold is exceptionally poorly understood and would be expected to vary as

833 a function of crustal composition, wet or dry conditions, and Q . The average of the means
834 of the posterior distributions of mid-crustal shear wave speed taken across eastern Tibet
835 is about 3.427 ± 0.050 km/s. Thus, using the 3.4 km/s threshold value, the mean value of
836 shear wave speed challenges the existence of pervasive mid-crustal partial melts across
837 the entirety of eastern Tibet. There are, however, several discrete regions that prefer
838 particularly low mid-crustal V_s . Figure 14b identifies the regions in which the inference
839 that $V_s < 3.4$ km/s is highly probable (or nearly so): the northern Songpan-Ganzi terrane,
840 the northern Chuandian terrane, and part of the central-to-northern Qiangtang terrane.
841 Most of these regions are coincident with high conductance areas from MT studies [*Wei*
842 *et al.*, 2001; *Bai et al.*, 2010]. The INDEPTH MT profile [*Wei et al.*, 2001; *Unsworth et*
843 *al.*, 2004] displays a conductive zone starting at about 25 km depth in the central
844 Qiangtang terrane, and the conductor deepens both northward and southward. In the north
845 Chuandian terrane, *Bai et al.* [2010] also observe a high conductive zone that begins at
846 about 25 km depth.

847 Therefore, determining with certainty whether V_s lies either above or below 3.4 km/s is
848 difficult using surface wave data alone. But, in summary, there is no compelling evidence
849 that V_s is less than 3.4 km/s pervasively across all of eastern Tibet, although such low
850 shear wave speeds are highly probable in three disjoint regions across the high plateau.
851 Thus, assuming that $V_s = 3.4$ km/s is an appropriate proxy for the onset of partial
852 melting, partial melt is probably not a pervasive feature of eastern Tibet except in three
853 disjoint regions (the northern Songpan-Ganzi terrane, the northern Chuandian terrane,
854 and part of the central-to-northern Qiangtang terrane) where it should be considered more

855 probable. But this inference is highly uncertain due to the uncertainty of the threshold
856 speed at which partial melt is likely to set on.

857 **7. Conclusions**

858 Based on Rayleigh (8 to 65 sec period) and Love (8 to 44 sec period) wave tomography
859 using seismic ambient noise, we mapped phase velocities across eastern Tibet and
860 surrounding regions using data recorded at PASSCAL and CEArray stations. A Bayesian
861 Monte Carlo inversion method was applied to generate posterior distributions of the 3-D
862 variation of V_{sv} and V_{sh} in the crust and uppermost mantle. Summarizing these
863 distributions with their means and standard deviations at each depth and location, we
864 showed that strong mid-crustal positive radial anisotropy ($V_{sh} > V_{sv}$) is observed across
865 all of eastern Tibet with a spatially averaged amplitude of $4.8\% \pm 1.4\%$ and terminates
866 abruptly near the border of the high plateau. Weaker ($-1.0\% \pm 1.4\%$) negative radial
867 anisotropy ($V_{sh} < V_{sv}$) is observed in the shallow crust beneath the Songpan-Ganzi
868 terrane and in the middle crust ($-2.8\% \pm 0.9\%$) near the border of the Tibetan plateau and
869 the Sichuan Basin. Positive mid-crustal radial anisotropy ($5.4\% \pm 1.4\%$) is observed in
870 the middle crust beneath the Sichuan Basin. Shear wave speed in the middle crust is
871 3.427 ± 0.050 km/s averaged across eastern Tibet.

872 We also queried the posterior distributions to determine which structural attributes are
873 highly probable and showed the following. (1) Positive mid-crustal radial anisotropy is
874 highly probable beneath the eastern high plateau. Lower crustal radial anisotropy is
875 determined more poorly than anisotropy in the middle crust. (2) Isotropic shear wave
876 speeds below 3.4 km/s are possible across most of the high plateau, but are highly
877 probable only beneath the northern Songpan-Ganzi, the northern Chuandian, and part of

878 the Qiangtang terranes. The relatively large uncertainty in V_s derives in part from the
879 trade-off between mid-crustal V_s and crustal thickness, which is poorly constrained by
880 surface wave data alone. (3) The crustal V_p/V_s ratio is a parameter that is fixed in the
881 inversion, and we set it in the crystalline crust to that of a Poisson solid: $V_p/V_s = 1.75$. If
882 a lower (higher) value were chosen, then the amplitude of radial anisotropy would have
883 decreased (increased) and mid-crustal V_s would have gone up (down). Vertically
884 averaged crustal V_p/V_s below 1.7 or above 1.8, however, would be hard to justify over
885 large areas of Tibet and if crustal V_p/V_s ranges between these values the resulting change
886 to radial anisotropy falls within estimated uncertainties.

887 A piece of (admittedly weak) evidence for partial melt in the middle crust would be shear
888 wave speeds at 35 km depth less than about 3.4 km/s [Yang *et al.*, 2012]. Although the
889 maximum likelihood shear wave speed across Tibet at this depth is 3.43 km/s, V_s below
890 3.4 km/s cannot be formally ruled out particularly if the crystalline crustal V_p/V_s value is
891 above 1.8. Such high values of V_p/V_s are characteristic of mafic mineralogy or partial
892 melt, but are unlikely for Tibet, at least systematically over large areas. Therefore, we
893 believe that mid-crustal partial melt is unlikely to exist pervasively across all of eastern
894 Tibet. However, it is most likely to exist in several smaller discrete regions, notably the
895 northern Songpan-Ganzi, the northern Chuandian, and part of the Qiangtang terranes,
896 where $V_s < 3.4$ km/s at 35 km depth is highly probable.

897 We interpret observations of positive mid-crustal radial anisotropy beneath eastern Tibet
898 and beneath the Sichuan Basin as evidence for planar mica sheets in the middle crust
899 oriented systematically such that their foliation planes are largely horizontal. Similarly,
900 the observation of negative mid-crustal radial anisotropy in the Longmenshan region

901 along the border separating Tibet from the Sichuan Basin is taken as evidence for planar
902 mica sheets oriented systematically such that their foliation planes are largely vertical.
903 We do not speculate on the nature of the deformation that produces this orientation of the
904 mica sheets, but do believe that the change in orientation of the mid-crustal foliation
905 plane near the eastern boundary of Tibet from dominantly horizontal to dominantly
906 vertical may result from the resistance force applied by the rigid lithosphere underlying
907 the Sichuan Basin. Finally, the negative anisotropy observed in the shallow crust beneath
908 the Songpan-Ganzi terrane and some other parts of eastern Tibet may be caused by faults
909 and cracks in the upper crust that have a substantial vertical component.

910 Some of the uncertainty in the estimates of radial anisotropy and in Voigt-averaged shear
911 wave speed V_s results from poor constraints on the V_p/V_s ratio in the crystalline crust, on
912 crustal thickness, and on radial anisotropy in the uppermost mantle. Future improvements
913 in estimates of crustal radial anisotropy and V_s will depend on developing improved
914 constraints on these structures. Earthquake surface wave tomography would improve
915 knowledge of radial anisotropy in the mantle and in the lowermost crust. Receiver
916 functions can be used to improve constraints on crustal thickness and perhaps also to
917 provide information about the average V_p/V_s across the crust.

918

919

920

921 **Acknowledgments.** The authors are particularly grateful for Peter Molnar's advice and
922 support. They also thank Bradley Hacker, David Okaya and Kevin Mahan for valuable

923 conversations as well as the PIs and team members of the PASSCAL experiments,
924 including the Hi-CLIMB, Namche Barwa, MIT-CHINA, Western Tibet,
925 ASCENT/INDEPTH IV experiments, as well as staff members from the PASSCAL
926 Instrument Center for collecting exceptionally valuable data in Tibet. The waveform data
927 from the Chinese stations were provided by the Data Management Centre of the China
928 National Seismic Network at the Institute of Geophysics, China Earthquake
929 Administration. In addition, the facilities of the IRIS Data Management System were
930 used to access some of the data used in this study. The IRIS DMS is funded through the
931 US National Science Foundation under Cooperative Agreement EAR-0552316. This
932 work was supported by US NSF-EAR award 0944022 and also was supported by a
933 Macquarie University Start-up Grant and New Staff Grant to Y. Yang.

934

935

936

937 **References:**

938

939 Acton, C. E., K. Priestley, V. K. Gaur, and S. S. Rai (2010), Group velocity tomography
940 of the Indo-Eurasian collision zone, *Journal of Geophysical Research: Solid*
941 *Earth*, 115(B12), n/a–n/a, doi:10.1029/2009JB007021.

942 Aki, K. and K. Kaminuma (1963), Phase velocity of Love waves in Japan, 1, Love wave
943 from the Aleutian shock of March 9, 1957, *Bull. Earthquake Res. Inst. Univ.*
944 *Tokyo*, 41, 243-260.

945

946 Aki, K. (1964), Study of Love and Rayleigh waves from earthquakes with fault plane
947 solutions or with known faulting Part 2. Application of the phase difference
948 method, *Bulletin of the Seismological Society of America*, 54(2), 529–558.

949 Babuška, V. (1991), *Seismic Anisotropy in the Earth*, Modern approaches in geophysics
950 v. 10, Kluwer Academic Publishers, Dordrecht, The Netherlands; Boston.

951 Babuška, V., J.-P. Montagner, J. Plomerová, and N. Girardin (1998), Age-dependent
952 Large-scale Fabric of the Mantle Lithosphere as Derived from Surface-wave

- 953 Velocity Anisotropy, *Pure appl. geophys.*, 151(2-4), 257–280,
954 doi:10.1007/s000240050114.
- 955 Bai, D. et al. (2010), Crustal deformation of the eastern Tibetan plateau revealed by
956 magnetotelluric imaging, *Nature Geoscience*, 3(5), 358–362,
957 doi:10.1038/ngeo830.
- 958 Barberini, V., L. Burlini, and A. Zappone (2007), Elastic properties, fabric and seismic
959 anisotropy of amphibolites and their contribution to the lower crust reflectivity,
960 *Tectonophysics*, 445(3–4), 227–244, doi:10.1016/j.tecto.2007.08.017.
- 961 Barmin, M. P., M. H. Ritzwoller, and A. L. Levshin (2001), A Fast and Reliable Method
962 for Surface Wave Tomography, *Pure and Applied Geophysics*, 158(8), 1351–
963 1375, doi:10.1007/PL00001225.
- 964 Barruol, G., and D. Mainprice (1993), 3-D seismic velocities calculated from lattice-
965 preferred orientation and reflectivity of a lower crustal section: examples of the
966 Val Sesia section (Ivrea zone, northern Italy), *Geophysical Journal International*,
967 115(3), 1169–1188, doi:10.1111/j.1365-246X.1993.tb01519.x.
- 968 Bassin, C., G. Laske, and G. Masters (2000), The Current Limits of Resolution for
969 Surface Wave Tomography in {North America}, *Eos*, 81.
- 970 Bensen, G. D., M. H. Ritzwoller, M. P. Barmin, A. L. Levshin, F. Lin, M. P. Moschetti,
971 N. M. Shapiro, and Y. Yang (2007), Processing seismic ambient noise data to
972 obtain reliable broad-band surface wave dispersion measurements, *Geophysical*
973 *Journal International*, 169(3), 1239–1260, doi:10.1111/j.1365-
974 246X.2007.03374.x.
- 975 Bensen, G. D., M. H. Ritzwoller, and Y. Yang (2009), A 3-D shear velocity model of the
976 crust and uppermost mantle beneath the United States from ambient seismic
977 noise, *Geophysical Journal International*, 177(3), 1177–1196,
978 doi:10.1111/j.1365-246X.2009.04125.x.
- 979 Brocher, T. M. (2005), Empirical Relations between Elastic Wavespeeds and Density in
980 the Earth's Crust, *Bulletin of the Seismological Society of America*, 95(6), 2081–
981 2092, doi:10.1785/0120050077.
- 982 Caldwell, W. B., S. L. Klemperer, S. S. Rai, and J. F. Lawrence (2009), Partial melt in
983 the upper-middle crust of the northwest Himalaya revealed by Rayleigh wave
984 dispersion, *Tectonophysics*, 477(1–2), 58–65, doi:10.1016/j.tecto.2009.01.013.
- 985 Chen, S. F., and C. J. L. Wilson (1996), Emplacement of the Longmen Shan Thrust—
986 Nappe Belt along the eastern margin of the Tibetan Plateau, *Journal of Structural*
987 *Geology*, 18(4), 413–430, doi:10.1016/0191-8141(95)00096-V.

- 988 Chen, Y., J. Badal, and J. Hu (2010), Love and Rayleigh Wave Tomography of the
989 Qinghai-Tibet Plateau and Surrounding Areas, *Pure Appl. Geophys.*, 167(10),
990 1171–1203, doi:10.1007/s00024-009-0040-1.
- 991 Cholach, P. Y., and D. R. Schmitt (2006), Intrinsic elasticity of a textured transversely
992 isotropic muscovite aggregate: Comparisons to the seismic anisotropy of schists
993 and shales, *Journal of Geophysical Research: Solid Earth*, 111(B9), n/a–n/a,
994 doi:10.1029/2005JB004158.
- 995 Cholach, P. Y., J. B. Molyneux, and D. R. Schmitt (2005), Flin Flon Belt seismic
996 anisotropy: elastic symmetry, heterogeneity, and shear-wave splitting, *Canadian
997 Journal of Earth Sciences*, 42(4), 533–554.
- 998 Christensen, N. I. (1996), Poisson's ratio and crustal seismology, *J. Geophys. Res.*,
999 101(B2), 3139–3156, doi:10.1029/95JB03446.
- 1000 Christensen, N. I., and W. D. Mooney (1995), Seismic velocity structure and composition
1001 of the continental crust: A global view, *Journal of Geophysical Research: Solid
1002 Earth*, 100(B6), 9761–9788, doi:10.1029/95JB00259.
- 1003 Cotte, N., H. Pedersen, M. Campillo, J. Mars, J. F. Ni, R. Kind, E. Sandvol, and W. Zhao
1004 (1999), Determination of the crustal structure in southern Tibet by dispersion and
1005 amplitude analysis of Rayleigh waves, *Geophysical Journal International*, 138(3),
1006 809–819, doi:10.1046/j.1365-246x.1999.00927.x.
- 1007 Crampin, S., and S. Chastin (2003), A review of shear wave splitting in the crack-critical
1008 crust, *Geophysical Journal International*, 155(1), 221–240, doi:10.1046/j.1365-
1009 246X.2003.02037.x.
- 1010 Duret, F., N. M. Shapiro, Z. Cao, V. Levin, P. Molnar, and S. Roecker (2010), Surface
1011 wave dispersion across Tibet: Direct evidence for radial anisotropy in the crust,
1012 *Geophys. Res. Lett.*, 37(16), L16306, doi:10.1029/2010GL043811.
- 1013 Ekström, G., and A. M. Dziewonski (1998), The unique anisotropy of the Pacific upper
1014 mantle, *Nature*, 394(6689), 168–172, doi:10.1038/28148.
- 1015 Figueiredo, J. J. S. de, J. Schleicher, R. R. Stewart, N. Dayur, B. Omoboya, R. Wiley, and
1016 A. William (2013), Shear wave anisotropy from aligned inclusions: ultrasonic
1017 frequency dependence of velocity and attenuation, *Geophys. J. Int.*,
1018 doi:10.1093/gji/ggs130. [online] Available from:
1019 <http://gji.oxfordjournals.org/content/early/2013/02/05/gji.ggs130> (Accessed 14
1020 February 2013)
- 1021 Frederiksen, A. W., and M. G. Bostock (2000), Modelling teleseismic waves in dipping
1022 anisotropic structures, *Geophysical Journal International*, 141(2), 401–412,
1023 doi:10.1046/j.1365-246x.2000.00090.x.

- 1024 Godfrey, N. J., N. I. Christensen, and D. A. Okaya (2000), Anisotropy of schists:
 1025 Contribution of crustal anisotropy to active source seismic experiments and shear
 1026 wave splitting observations, *Journal of Geophysical Research: Solid Earth*,
 1027 *105*(B12), 27991–28007, doi:10.1029/2000JB900286.
- 1028 Guo, Z., X. Gao, H. Yao, J. Li, and W. Wang (2009), Midcrustal low-velocity layer
 1029 beneath the central Himalaya and southern Tibet revealed by ambient noise array
 1030 tomography, *Geochemistry, Geophysics, Geosystems*, *10*(5), n/a–n/a,
 1031 doi:10.1029/2009GC002458.
- 1032 Hall, S. A., J.-M. Kendall, J. Maddock, and Q. Fisher (2008), Crack density tensor
 1033 inversion for analysis of changes in rock frame architecture, *Geophysical Journal
 1034 International*, *173*(2), 577–592, doi:10.1111/j.1365-246X.2008.03748.x.
- 1035 Huang, H., H. Yao, and R. D. van der Hilst (2010), Radial anisotropy in the crust of SE
 1036 Tibet and SW China from ambient noise interferometry, *Geophys. Res. Lett.*, *37*, 5
 1037 PP., doi:201010.1029/2010GL044981.
- 1038 James, M. B., and M. H. Ritzwoller (1999), *Feasibility of truncated perturbation
 1039 expansions to approximate Rayleigh wave eigenfrequencies and eigenfunctions in
 1040 heterogeneous.*
- 1041 Jiang, M., A. Galve, A. Hirn, B. de Voogd, M. Laigle, H. P. Su, J. Diaz, J. C. Lepine, and
 1042 Y. X. Wang (2006), Crustal thickening and variations in architecture from the
 1043 Qaidam basin to the Qang Tang (North-Central Tibetan Plateau) from wide-
 1044 angle reflection seismology, *Tectonophysics*, *412*(3-4), 121–140,
 1045 doi:10.1016/j.tecto.2005.09.011.
- 1046 Jiang, M., S. Zhou, E. Sandvol, X. Chen, X. Liang, Y. J. Chen, and W. Fan (2011), 3-D
 1047 lithospheric structure beneath southern Tibet from Rayleigh-wave tomography
 1048 with a 2-D seismic array, *Geophysical Journal International*, *185*(2), 593–608,
 1049 doi:10.1111/j.1365-246X.2011.04979.x.
- 1050 Kanamori, H., and D. L. Anderson (1977), Importance of physical dispersion in surface
 1051 wave and free oscillation problems: Review, *Reviews of Geophysics*, *15*(1), 105–
 1052 112, doi:10.1029/RG015i001p00105.
- 1053 Karato, S. (1993), Importance of anelasticity in the interpretation of seismic tomography,
 1054 *Geophysical Research Letters*, *20*(15), 1623–1626, doi:10.1029/93GL01767.
- 1055 Kawakatsu, H., P. Kumar, Y. Takei, M. Shinohara, T. Kanazawa, E. Araki, and K.
 1056 Suyehiro (2009), Seismic Evidence for Sharp Lithosphere-Asthenosphere
 1057 Boundaries of Oceanic Plates, *Science*, *324*(5926), 499–502,
 1058 doi:10.1126/science.1169499.
- 1059 Kennett, B. L. N., E. R. Engdahl, and R. Buland (1995), Constraints on seismic velocities
 1060 in the Earth from traveltimes, *Geophysical Journal International*, *122*(1), 108–
 1061 124, doi:10.1111/j.1365-246X.1995.tb03540.x.

- 1062 Kitamura, K. (2006), Constraint of lattice-preferred orientation (LPO) on V_p
1063 anisotropy of amphibole-rich rocks, *Geophysical Journal International*, 165(3),
1064 1058–1065, doi:10.1111/j.1365-246X.2006.02961.x.
- 1065 Leary, P. C., S. Crampin, and T. V. McEvilly (1990), Seismic fracture anisotropy in the
1066 Earth's crust: An overview, *Journal of Geophysical Research: Solid Earth*,
1067 95(B7), 11105–11114, doi:10.1029/JB095iB07p11105.
- 1068 Levin, V., and J. Park (1997), P-SH conversions in a flat-layered medium with
1069 anisotropy of arbitrary orientation, *Geophysical Journal International*, 131(2),
1070 253–266, doi:10.1111/j.1365-246X.1997.tb01220.x.
- 1071 Levshin, A. L., M. H. Ritzwoller, and L. I. Ratnikova (1994), The nature and cause of
1072 polarization anomalies of surface waves crossing northern and central Eurasia,
1073 *Geophysical Journal International*, 117(3), 577–590, doi:10.1111/j.1365-
1074 246X.1994.tb02455.x.
- 1075 Levshin, A. L., M. H. Ritzwoller, and N. M. Shapiro (2005), The use of crustal higher
1076 modes to constrain crustal structure across Central Asia, *Geophysical Journal*
1077 *International*, 160(3), 961–972, doi:10.1111/j.1365-246X.2005.02535.x.
- 1078 Levshin, A. L., X. Yang, M. P. Barmin, and M. H. Ritzwoller (2010), Midperiod
1079 Rayleigh wave attenuation model for Asia, *Geochemistry, Geophysics,*
1080 *Geosystems*, 11(8), n/a–n/a, doi:10.1029/2010GC003164.
- 1081 Li, H., W. Su, C.-Y. Wang, and Z. Huang (2009), Ambient noise Rayleigh wave
1082 tomography in western Sichuan and eastern Tibet, *Earth and Planetary Science*
1083 *Letters*, 282(1–4), 201–211, doi:10.1016/j.epsl.2009.03.021.
- 1084 Lin, F.-C., M. P. Moschetti, and M. H. Ritzwoller (2008), Surface wave tomography of
1085 the western United States from ambient seismic noise: Rayleigh and Love wave
1086 phase velocity maps, *Geophysical Journal International*, 173(1), 281–298,
1087 doi:10.1111/j.1365-246X.2008.03720.x.
- 1088 Lin, F.-C., M. H. Ritzwoller, and R. Snieder (2009), Eikonal tomography: surface wave
1089 tomography by phase front tracking across a regional broad-band seismic array,
1090 *Geophysical Journal International*, 177(3), 1091–1110, doi:10.1111/j.1365-
1091 246X.2009.04105.x.
- 1092 Lloyd, G. E., R. W. H. Butler, M. Casey, and D. Mainprice (2009), Mica, deformation
1093 fabrics and the seismic properties of the continental crust, *Earth and Planetary*
1094 *Science Letters*, 288(1–2), 320–328, doi:10.1016/j.epsl.2009.09.035.
- 1095 Maceira, M., S. R. Taylor, C. J. Ammon, X. Yang, and A. A. Velasco (2005), High-
1096 resolution Rayleigh wave slowness tomography of central Asia, *Journal of*
1097 *Geophysical Research: Solid Earth*, 110(B6), n/a–n/a,
1098 doi:10.1029/2004JB003429.

- 1099 Mahan, K. (2006), Retrograde mica in deep crustal granulites: Implications for crustal
1100 seismic anisotropy, *Geophys. Res. Lett.*, 33(24), L24301,
1101 doi:10.1029/2006GL028130.
- 1102 Masters, G., M. P. Barmine, and S. Kientz (2007), Mineos user's manual, in
1103 Computational Infrastructure for Geodynamics, Calif. Inst. of Technol., Pasadena
1104
- 1105 McEvelly, T. V. (1964), Central U.S. crust—Upper mantle structure from Love and
1106 Rayleigh wave phase velocity inversion, *Bulletin of the Seismological Society of*
1107 *America*, 54(6A), 1997–2015.
- 1108 Mechie, J., R. Kind, and J. Saul (2011), The seismological structure of the Tibetan
1109 Plateau crust and mantle down to 700 km depth, *Geological Society, London,*
1110 *Special Publications*, 353(1), 109–125, doi:10.1144/SP353.7.
- 1111 Mechie, J. et al. (2012), Crustal shear (S) velocity and Poisson's ratio structure along the
1112 INDEPTH IV profile in northeast Tibet as derived from wide-angle seismic data,
1113 *Geophysical Journal International*, 191(2), 369–384, doi:10.1111/j.1365-
1114 246X.2012.05616.x.
- 1115 Montagner, J.-P., and T. Tanimoto (1991), Global upper mantle tomography of seismic
1116 velocities and anisotropies, *Journal of Geophysical Research: Solid Earth*,
1117 96(B12), 20337–20351, doi:10.1029/91JB01890.
- 1118 Moschetti, M. P., and M. H. R., F.-C. Lin, and Y. Yang (2010), Crustal shear wave
1119 velocity structure of the western United States inferred from ambient seismic
1120 noise and earthquake data, *J. Geophys. Res.*, 115, 20 PP., doi:2010
1121 10.1029/2010JB007448.
- 1122 Moschetti, M. P., M. H. Ritzwoller, F. Lin, and Y. Yang (2010), Seismic evidence for
1123 widespread western-US deep-crustal deformation caused by extension, *Nature*,
1124 464(7290), 885–889, doi:10.1038/nature08951.
- 1125 Nettles, M., and A. M. Dziewoński (2008), Radially anisotropic shear velocity structure
1126 of the upper mantle globally and beneath North America, *J. Geophys. Res.*, 113,
1127 27 PP., doi:200810.1029/2006JB004819.
- 1128 Nishizawa, O., and T. Yoshino (2001), Seismic velocity anisotropy in mica-rich rocks: an
1129 inclusion model, *Geophysical Journal International*, 145(1), 19–32,
1130 doi:10.1111/j.1365-246X.2001.00331.x.
- 1131 Okaya, D. A., and T. V. McEvelly (2003), Elastic wave propagation in anisotropic crustal
1132 material possessing arbitrary internal tilt, *Geophysical Journal International*,
1133 153(2), 344–358, doi:10.1046/j.1365-246X.2003.01896.x.
- 1134 Rapine, R., F. Tilmann, M. West, J. Ni, and A. Rodgers (2003), Crustal structure of
1135 northern and southern Tibet from surface wave dispersion analysis, *Journal of*

- 1136 *Geophysical Research: Solid Earth*, 108(B2), n/a–n/a,
1137 doi:10.1029/2001JB000445.
- 1138 Shapiro, N. M., and M. H. Ritzwoller (2002), Monte-Carlo inversion for a global shear-
1139 velocity model of the crust and upper mantle, *Geophysical Journal International*,
1140 151(1), 88–105, doi:10.1046/j.1365-246X.2002.01742.x.
- 1141 Shapiro, N. M., M. H. Ritzwoller, P. Molnar, and V. Levin (2004), Thinning and Flow of
1142 Tibetan Crust Constrained by Seismic Anisotropy, *Science*, 305(5681), 233–236,
1143 doi:10.1126/science.1098276.
- 1144 Shen, W., M. H. Ritzwoller, and V. Schulte-Pelkum (2013a), A 3-D model of the crust
1145 and uppermost mantle beneath the Central and Western US by joint inversion of
1146 receiver functions and surface wave dispersion, *Journal of Geophysical Research:*
1147 *Solid Earth*, n/a–n/a, doi:10.1029/2012JB009602.
- 1148 Shen, W., M. H. Ritzwoller, V. Schulte-Pelkum, and F.-C. Lin (2013b), Joint inversion of
1149 surface wave dispersion and receiver functions: a Bayesian Monte-Carlo
1150 approach, *Geophys. J. Int.*, 192(2), 807–836, doi:10.1093/gji/ggs050.
- 1151 Sherrington, H. F., G. Zandt, and A. Frederiksen (2004), Crustal fabric in the Tibetan
1152 Plateau based on waveform inversions for seismic anisotropy parameters, *Journal*
1153 *of Geophysical Research: Solid Earth*, 109(B2), n/a–n/a,
1154 doi:10.1029/2002JB002345.
- 1155 Sloan, R. A., J. A. Jackson, D. McKenzie, and K. Priestley (2011), Earthquake depth
1156 distributions in central Asia, and their relations with lithosphere thickness,
1157 shortening and extension, *Geophys. J. Int.*, 185(1), 1–29, doi:10.1111/j.1365-
1158 246X.2010.04882.x.
- 1159 Takeuchi, H., Y. Hamano, and Y. Hasegawa (1968), Rayleigh- and Love-wave
1160 discrepancy and the existence of magma pockets in the upper mantle, *Journal of*
1161 *Geophysical Research*, 73(10), 3349–3350, doi:10.1029/JB073i010p03349.
- 1162 Tatham, D. J., G. E. Lloyd, R. W. H. Butler, and M. Casey (2008), Amphibole and lower
1163 crustal seismic properties, *Earth and Planetary Science Letters*, 267(1–2), 118–
1164 128, doi:10.1016/j.epsl.2007.11.042.
- 1165 Trampert, J., and J. H. Woodhouse (1995), Global phase velocity maps of Love and
1166 Rayleigh waves between 40 and 150 seconds, *Geophysical Journal International*,
1167 122(2), 675–690, doi:10.1111/j.1365-246X.1995.tb07019.x.
- 1168 Unsworth, M., W. Wenbo, A. G. Jones, S. Li, P. Bedrosian, J. Booker, J. Sheng, D. Ming,
1169 and T. Handong (2004), Crustal and upper mantle structure of northern Tibet
1170 imaged with magnetotelluric data, *Journal of Geophysical Research: Solid Earth*,
1171 109(B2), n/a–n/a, doi:10.1029/2002JB002305.

- 1172 Valcke, S. L. A., M. Casey, G. E. Lloyd, J.-M. Kendall, and Q. J. Fisher (2006), Lattice
 1173 preferred orientation and seismic anisotropy in sedimentary rocks, *Geophysical*
 1174 *Journal International*, 166(2), 652–666, doi:10.1111/j.1365-246X.2006.02987.x.
- 1175 Vergne, J., G. Wittlinger, Q. Hui, P. Tapponnier, G. Poupinet, J. Mei, G. Herquel, and A.
 1176 Paul (2002), Seismic evidence for stepwise thickening of the crust across the NE
 1177 Tibetan plateau, *Earth and Planetary Science Letters*, 203(1), 25–33,
 1178 doi:10.1016/S0012-821X(02)00853-1.
- 1179 Villaseñor, A., M. H. Ritzwoller, A. L. Levshin, M. P. Barmin, E. R. Engdahl, W.
 1180 Spakman, and J. Trampert (2001), Shear velocity structure of central Eurasia from
 1181 inversion of surface wave velocities, *Physics of the Earth and Planetary Interiors*,
 1182 123(2-4), 169–184, doi:10.1016/S0031-9201(00)00208-9.
- 1183 Wang, C.-Y., L. Zhu, H. Lou, B.-S. Huang, Z. Yao, and X. Luo (2010), Crustal
 1184 thicknesses and Poisson’s ratios in the eastern Tibetan Plateau and their tectonic
 1185 implications, *J. Geophys. Res.*, 115(B11), B11301, doi:10.1029/2010JB007527.
- 1186 Ward, D., K. Mahan, and V. Schulte-Pelkum (2012), Roles of quartz and mica in seismic
 1187 anisotropy of mylonites, *Geophysical Journal International*, 190(2), 1123–1134,
 1188 doi:10.1111/j.1365-246X.2012.05528.x.
- 1189 Wei, W. et al. (2001), Detection of Widespread Fluids in the Tibetan Crust by
 1190 Magnetotelluric Studies, *Science*, 292(5517), 716–719,
 1191 doi:10.1126/science.1010580.
- 1192 Wendt, A. S., I. O. Bayuk, S. J. Covey-Crump, R. Wirth, and G. E. Lloyd (2003), An
 1193 experimental and numerical study of the microstructural parameters contributing
 1194 to the seismic anisotropy of rocks, *Journal of Geophysical Research: Solid Earth*,
 1195 108(B8), n/a–n/a, doi:10.1029/2002JB001915.
- 1196 Xie, J., W. Shen, M.H. Ritzwoller, Y. Yang, L. Zhou, Y. Zheng (2012), Imaging crustal
 1197 anisotropy in eastern Tibet and South China using ambient noise and earthquake
 1198 data, *AGU fall meeting*, 2012, T33D-2683
- 1199 Xie, J., and M.H. Ritzwoller (2013), The joint interpretation of crustal radial and
 1200 azimuthal anisotropy to determine the symmetry axes of the elastic tensor, in
 1201 preparation.
 1202
- 1203 Xu, L., S. Rondenay, and R. D. van der Hilst (2007), Structure of the crust beneath the
 1204 southeastern Tibetan Plateau from teleseismic receiver functions, *Physics of the*
 1205 *Earth and Planetary Interiors*, 165(3–4), 176–193,
 1206 doi:10.1016/j.pepi.2007.09.002.
- 1207 Yang, Y. et al. (2010), Rayleigh wave phase velocity maps of Tibet and the surrounding
 1208 regions from ambient seismic noise tomography, *Geochemistry, Geophysics,*
 1209 *Geosystems*, 11(8), n/a–n/a, doi:10.1029/2010GC003119.

1210 Yang, Y., M. H. Ritzwoller, Y. Zheng, W. Shen, A. L. Levshin, and Z. Xie (2012), A
1211 synoptic view of the distribution and connectivity of the mid-crustal low velocity
1212 zone beneath Tibet, *J. Geophys. Res.*, *117*, 20 PP.,
1213 doi:201210.1029/2011JB008810.

1214 Yao, H., C. Beghein, and R. D. van der Hilst (2008), Surface-wave array tomography in
1215 SE Tibet from ambient seismic noise and two-station analysis - II. Crustal and
1216 upper-mantle structure, *Geophysical Journal International*, *173*, 205–219.

1217 Yao, H., R. D. van der Hilst, and J.-P. Montagner (2010), Heterogeneity and anisotropy
1218 of the lithosphere of SE Tibet from surface wave array tomography, *J. Geophys.*
1219 *Res.*, *115*(B12), B12307, doi:10.1029/2009JB007142.

1220 Yue, H. et al. (2012), Lithospheric and upper mantle structure of the northeastern Tibetan
1221 Plateau, *J. Geophys. Res.*, *117*(B5), B05307, doi:10.1029/2011JB008545.

1222 Zandt, G., and C. J. Ammon (1995), Continental crust composition constrained by
1223 measurements of crustal Poisson's ratio, , *Published online: 09 March 1995*; |
1224 doi:10.1038/374152a0, 374(6518), 152–154, doi:10.1038/374152a0.

1225 Zhang, Z. M., J. G. Liou, and R. G. Coleman (1984), An outline of the plate tectonics of
1226 China, *Geological Society of America Bulletin*, *95*(3), 295–312,
1227 doi:10.1130/0016-7606(1984)95<295:AOOTPT>2.0.CO;2.

1228 Zhang, P., Q. Deng, G. Zhang, J. Ma, W. Gan, W. Min, F. Mao, and Q. Wang (2003),
1229 Active tectonic blocks and strong earthquakes in the continent of China, *Sci.*
1230 *China Ser. D-Earth Sci.*, *46*(2), 13–24, doi:10.1360/03dz0002.

1231 Zhang, P.-Z., X. Wen, Z.-K. Shen, and J. Chen (2010), Oblique, High-Angle, Listric-
1232 Reverse Faulting and Associated Development of Strain: The Wenchuan
1233 Earthquake of May 12, 2008, Sichuan, China, *Annual Review of Earth and*
1234 *Planetary Sciences*, *38*(1), 353–382, doi:10.1146/annurev-earth-040809-152602.

1235 Zheng, X.-F., Z.-X. Yao, J.-H. Liang, and J. Zheng (2010), The Role Played and
1236 Opportunities Provided by IGP DMC of China National Seismic Network in
1237 Wenchuan Earthquake Disaster Relief and Researches, *Bulletin of the*
1238 *Seismological Society of America*, *100*(5B), 2866–2872,
1239 doi:10.1785/0120090257.

1240 Zhou, L., J. Xie, W. Shen, Y. Zheng, Y. Yang, H. Shi, and M. H. Ritzwoller (2012), The
1241 structure of the crust and uppermost mantle beneath South China from ambient
1242 noise and earthquake tomography, *Geophysical Journal International*, *189*(3),
1243 1565–1583, doi:10.1111/j.1365-246X.2012.05423.x.

1244
1245
1246
1247

1248
 1249
 1250
 1251
 1252
 1253
 1254
 1255
 1256
 1257
 1258
 1259
 1260
 1261
 1262
 1263
 1264
 1265
 1266
 1267
 1268
 1269
 1270
 1271
 1272
 1273
 1274
 1275
 1276
 1277
 1278

Table 1. Model parameter constraints

	Model parameter	Perturbation	Reference model
Sedimentary layer	Sediment thickness Vsv in sediment Vsh in sediment	+/- 100% +/- 1.0 km/s equals to Vsv	CRUST2.0
Crystalline crustal layer	Crustal thickness 5 Vsv B-splines* 5 Vsh B-splines*	+/- 10% +/- 20% +/- 20%	<i>Shapiro & Ritzwoller</i> [2002]
Mantle layer to 150 km	5 Vsv B-splines Anisotropy	+/- 20% 0	<i>Shapiro & Ritzwoller</i> [2002]

1279 * $\Delta v/\Delta h \geq 0$ or $-1/70 \text{ s}^{-1} \leq \Delta v/\Delta h < 0$
 1280

1281
1282
1283
1284
1285
1286
1287
1288
1289
1290
1291
1292
1293
1294
1295
1296
1297
1298
1299
1300
1301
1302
1303
1304
1305
1306
1307
1308
1309
1310

1311 **Figure Caption**

1312
1313 **Figure 1.** (a) Reference map of the study region in which red lines indicate the
1314 boundaries of major geological units and basins [Zhang *et al.*, 1984, 2003]. The white
1315 contour outlines what we refer to as the Longmenshan region. The blue line is the path
1316 between stations X4.F17 and X4.D26 referenced in Fig. 2. Points A, B, C, and D indicate
1317 sample points referenced in Figs. 6, 7, 13, 16, and 17. (b) Locations of seismic stations
1318 used in this study. Red and black triangles are stations used to measure Love wave
1319 dispersion, while blue and black triangles indicate stations used for Rayleigh wave
1320 measurements.

1321 **Figure 2.** (a) Example of Rayleigh wave (blue, vertical-vertical, Z-Z) and Love wave
1322 (red, transverse-transverse, T-T) cross-correlations for a pair of stations (X4.F17,

1323 X4.D26) located in the Qiantang terrane (Fig. 1a), band pass filtered between 5 and 100
1324 sec period. (b) Observed Rayleigh and Love wave phase speed curves measured from the
1325 cross-correlations are presented as 1 standard deviation (1σ) error bars (red-Love, blue-
1326 Rayleigh). Inverting these data for an isotropic model ($V_s = V_{sh} = V_{sv}$) produces the
1327 best fitting green curves, which demonstrates a systematic misfit to the data
1328 (predominantly the Love waves) and a Rayleigh-Love discrepancy. Allowing crustal
1329 anisotropy ($V_{sh} \neq V_{sv}$), produces the blue and red dispersion curves that fit the data.

1330 **Figure 3.** Example estimated Rayleigh (a,b) and Love (c,d) wave phase speed maps at 10
1331 (a,c) and 40 sec (b,d) period determined from ambient noise cross-correlations.

1332 **Figure 4.** Uncertainties (1σ) in the Rayleigh and Love wave phase speed maps averaged
1333 across the study region estimated using the eikonal tomography method of *Lin et al.* [
1334 2009].

1335 **Figure 5.** Representation of the parameterization used across the study region. In the
1336 crust, five B-splines (1-5) are used to represent V_{sv} , but three B-splines (2-4) are used to
1337 represent V_{sh} . In the mantle, five B-splines are estimated for V_{sv} but V_{sh} is derived from
1338 the strength of radial anisotropy in the model of *Shapiro and Ritzwoller* [2002]. A total of
1339 16 parameters represent the model at each spatial location.

1340 **Figure 6.** Prior (white histograms) and posterior distributions for V_{sv} (blue), V_{sh} (red)
1341 and radial anisotropy (green, $(V_{sh}-V_{sv})/V_s$, in percent) at 20, 35, and 50 km depth for
1342 point B in the Qiantang terrane (Fig. 1a). The mean and standard deviation for each
1343 posterior distribution are shown in each panel.

1344 **Figure 7.** Examples of dispersion curves and estimated radially anisotropy for four
1345 spatial locations (A, B, C, D) identified in Fig. 1a. (a) Point A (98.5, 36.0) near the
1346 eastern edge of the Qaidam Basin. Local Rayleigh and Love wave phase speed curves
1347 presented as one standard deviation (1σ) error bars. Predictions from the average of the
1348 anisotropic model distribution in (b) are shown as solid lines and green lines are
1349 predictions from the Voigt-averaged isotropic V_s model. Misfits (defined as $\chi = \sqrt{S/N}$
1350 where S is defined in Eq. 3) correlated with anisotropic and isotropic models are shown at
1351 the upper left corner. (b) Point A (cont.). Inversion result in which the one standard

1352 deviation (1σ) model distributions are shown with the grey corridors for V_{sh} and V_{sv} ,
1353 with the average of each ensemble plotted with bold blue (V_{sv}) and red (V_{sh}) lines. The
1354 model ensembles are nearly coincident in the crust, consistent with an isotropic crust. (c)
1355 & (d) Point B (96.5, 32.5) in the Qiangtang terrane where the central crust has strong
1356 positive radial anisotropy between 20 and 50 km depth and weak negative anisotropy
1357 above about 15 km depth. (e) & (f) Point C (105.0, 30.0) in the Sichuan Basin where the
1358 central crust has strong positive radial anisotropy between depths of 10 and 25 km. (g) &
1359 (h) Point D (102.5, 30.0) between Tibet and the Sichuan Basin where the central crust has
1360 strong negative radial anisotropy between 20 and 50 km depth.

1361 **Figure 8.** The average of the posterior distributions of (a) V_{sv} , (b) V_{sh} , and (c) V_s at 35
1362 km depth in km/s, which is in the middle crust beneath the Tibetan Plateau. Regions with
1363 very low velocities (<3.4 km/s) are encircled by white contours. (d) The average of the
1364 posterior distribution of crustal thickness in km.

1365 **Figure 9.** Maps of the mean of the posterior distribution for estimates of radial anisotropy
1366 at (a) 10 km depth, (b) 35 km depth, and (c) 90% of the depth to Moho in the lowermost
1367 crust. Radial anisotropy units are the percent difference between V_{sh} and V_{sv} at each
1368 location and depth: $(V_{sh}-V_{sv})/V_s$, where V_s is the Voigt-averaged shear wave speed.
1369 Blue lines in (a) identify the locations of the vertical cross-sections in Fig. 10.

1370 **Figure 10.** Vertical cross-sections of (upper left) V_{sv} , (middle left) V_{sh} , and (lower left)
1371 radial anisotropy along profile A (Fig. 9a), taken from the mean of the posterior
1372 distribution at each location and depth. Topography is shown at the top of each panel as
1373 are locations of geological-block boundaries (SG: Songpan-Ganzi terrane, CD:
1374 Chuandian terrane, LS: Lhasa terrane, QL: Qilian terrane, SCB: Sichuan Basin, SYN:
1375 South Yunnan region, YZ: Yangtze craton). Crustal shear velocities are presented in
1376 absolute units (km/s), radial anisotropy is presented as the percent difference between
1377 V_{sh} and V_{sv} ($(V_{sh}-V_{sv})/V_s$), and mantle velocities are percentage perturbations relative
1378 to 4.4 km/s. (Right) Radial anisotropy is presented beneath profiles B, C, and D (Fig. 9a).

1379 **Figure 11.** Maps of the one standard deviation (i.e., error) of the posterior distribution for
1380 estimates of radial anisotropy at (a) 10 km depth, (b) 35 km depth, and (c) 90% of the

1381 depth to Moho. Results are in the same units as radial anisotropy, not in the percentage of
1382 radial anisotropy at each point.

1383 **Figure 12.** Plots of the spatial distribution of the mean of the posterior distributions of
1384 radial anisotropy across (a) the Songpan-Ganzi terrane between depths of 5 and 15 km, (b)
1385 eastern Tibet at depths between 30 and 40 km, (c) the Sichuan Basin at depths between 5
1386 and 20 km, and (d) the Longmenshan region between eastern Tibet and the Sichuan Basin
1387 between 25 and 35 km. (e) The distribution of the mean of the posterior distribution for
1388 Voigt-averaged shear wave speed V_s across eastern Tibet between depths of 30 and 40
1389 km.

1390 **Figure 13.** (a) Percent of accepted models at each location with positive radial anisotropy
1391 ($V_{sh} > V_{sv}$) at 35 km depth. Values of 2.2%, 15.8%, 84.2%, and 97.8% are contoured by
1392 black lines, which are correlated with the position of $\pm 1 \sigma$ and $\pm 2 \sigma$ in a Gaussian
1393 distribution. (b) Prior (white histogram in the background) and posterior (colored
1394 histogram) distributions of radial anisotropy ($(V_{sh}-V_{sv})/V_s$, in percent) at 35 km depth
1395 for locations A, B, and D of Fig. 1a. The red line indicates the position of zero radial
1396 anisotropy. The percent of models with positive radial anisotropy is indicated to the right
1397 of each panel. (c) Same as (a), but for positive radial anisotropy at 10 km depth. (d) Same
1398 as (a), but for positive radial anisotropy at 15 km depth.

1399 **Figure 14.** Similar to Fig. 13a, but this figure is the percentage of accepted models at
1400 each location with Voigt-averaged $V_s > 3.4$ km/s at 35 km depth. (b) Same as (a), but for
1401 $V_s < 3.4$ km/s at 35 km depth.

1402 **Figure 15.** The spatially averaged effect of crustal parameterization of radial anisotropy
1403 on the mean and standard deviation of radial anisotropy averaged across the Tibetan crust.
1404 Crustal radial anisotropy and uncertainty are presented as error bars as a function of (a)
1405 absolute depth and (b) depth measured as a ratio of crustal thickness, averaged over the
1406 study region where surface elevation is more than 3 km (black contour in Fig. 1a). The
1407 middle of each error bar is the average amplitude of radial anisotropy ($(V_{sh}-V_{sv})/V_s$, in
1408 percent) and the half-width of the error bar is the average one-standard deviation
1409 uncertainty. Blue bars result from the more tightly constrained inversion (uppermost and
1410 lowermost crust are approximately isotropic, $V_{sh}=V_{sv}$ for crustal B-splines 1 and 5 in

1411 Fig. 5, but V_{sh} and V_{sv} can differ for splines 2 to 4). Red bars are results from the less
1412 constrained inversion (radial anisotropy is allowed across the entire crust, V_{sv} may differ
1413 from V_{sh} for all five crustal B-splines).

1414 **Figure 16.** Trade-off between the depth-averaged (from Moho to 150 km) amplitude of
1415 mantle radial anisotropy used in the inversion and (a) the depth-averaged (± 5 km around
1416 the middle crust) mid-crustal radial anisotropy and (b) the depth-averaged (± 5 km around
1417 the middle crust) mid-crustal Voigt-averaged V_s . Each dot is the depth-averaged value
1418 and half-widths of the error bars are the depth-averaged one-standard deviation
1419 uncertainty. Both come from the inversion with a given mantle radial anisotropy at
1420 location D identified in Fig. 1a. The triangles are the values in our final model. (c)&(d)
1421 Similar to (a)&(b), but showing the trade-off between the crustal thickness and (c) the
1422 depth-averaged mid-crustal radial anisotropy and (d) the depth-averaged mid-crustal
1423 Voigt-averaged V_s .

1424 **Figure 17.** Similar to Fig. 16, but for the trade-off between the fixed value of the crustal
1425 V_p/V_s used in the inversion and (a) the depth-averaged (from 30 to 40 km) crustal radial
1426 anisotropy and (b) the depth-averaged (from 30 to 40 km) mid-crustal Voigt-averaged V_s .
1427 Values are from inversion with a given crustal V_p/V_s at location B identified in Fig. 1a.

1428 **Figure 18.** (a) Pictorial definition of the rotation angle φ for a hexagonally symmetric
1429 system. (b) Simulated estimate of the normalized strength of radial anisotropy, $(V_{sh}-$
1430 $V_{sv})/V_s$, plotted as a function of rotation angle φ .

1431

1432

Figure 1

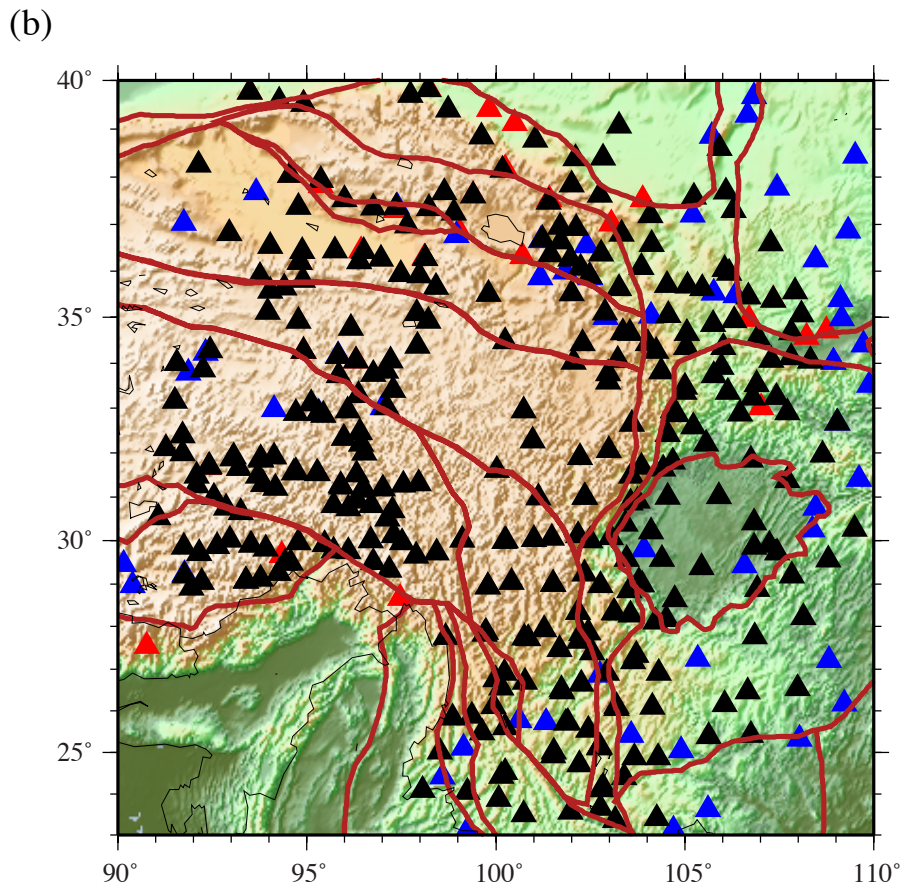
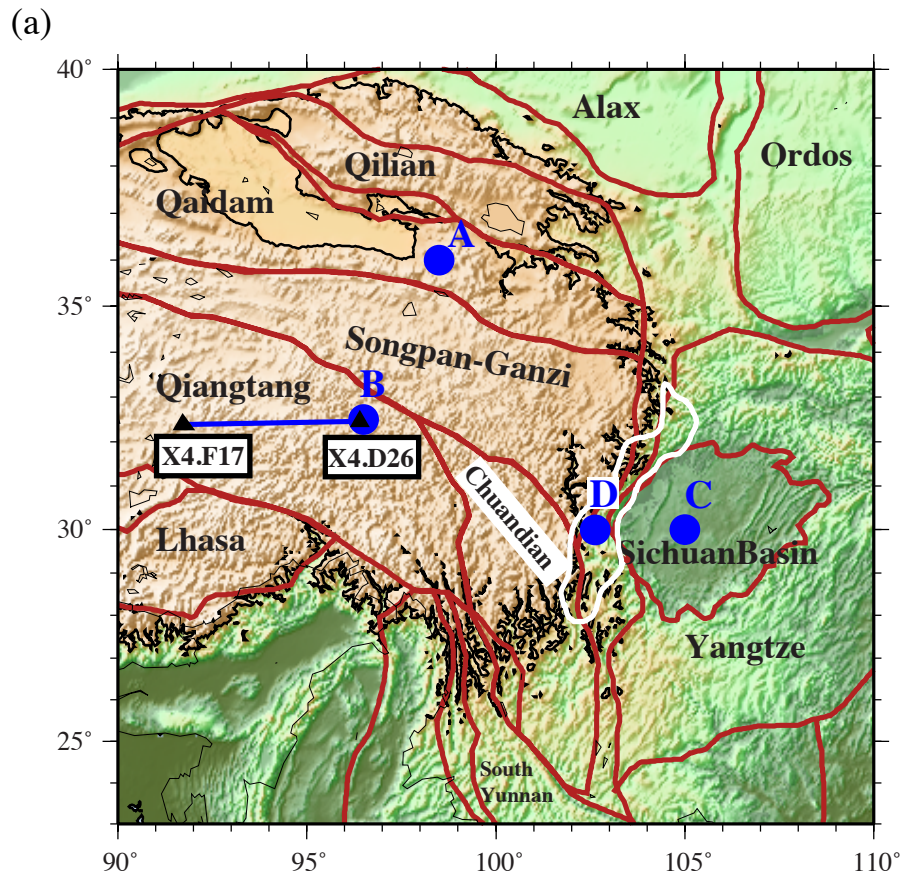


Figure 2

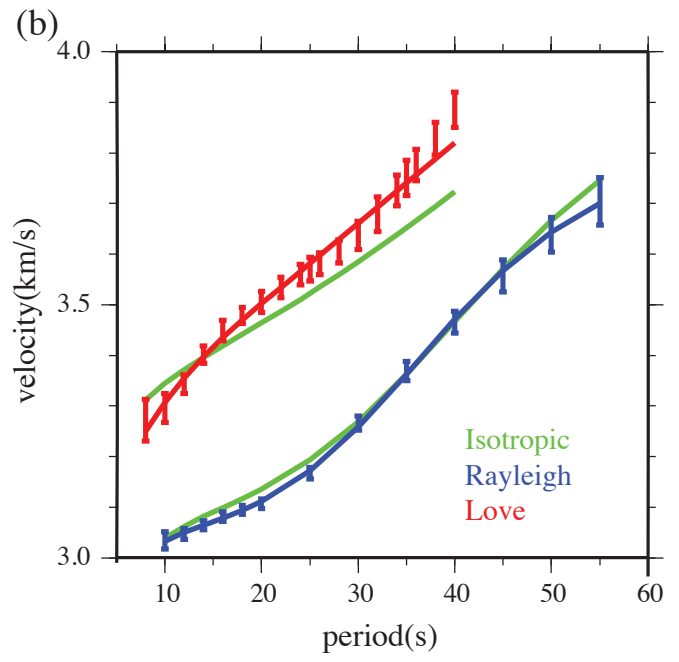
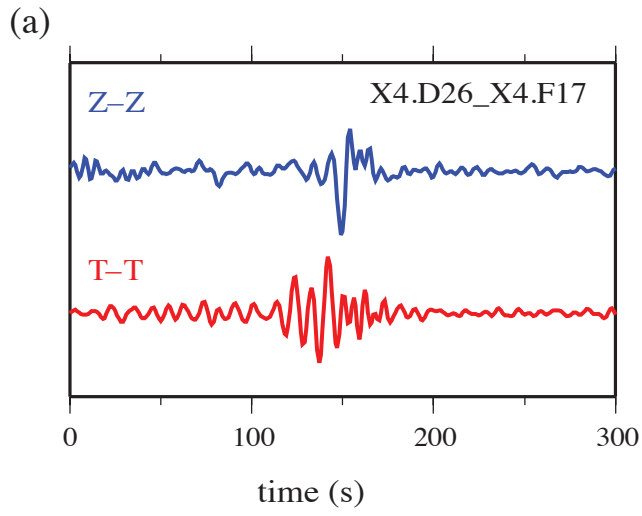


Figure 3

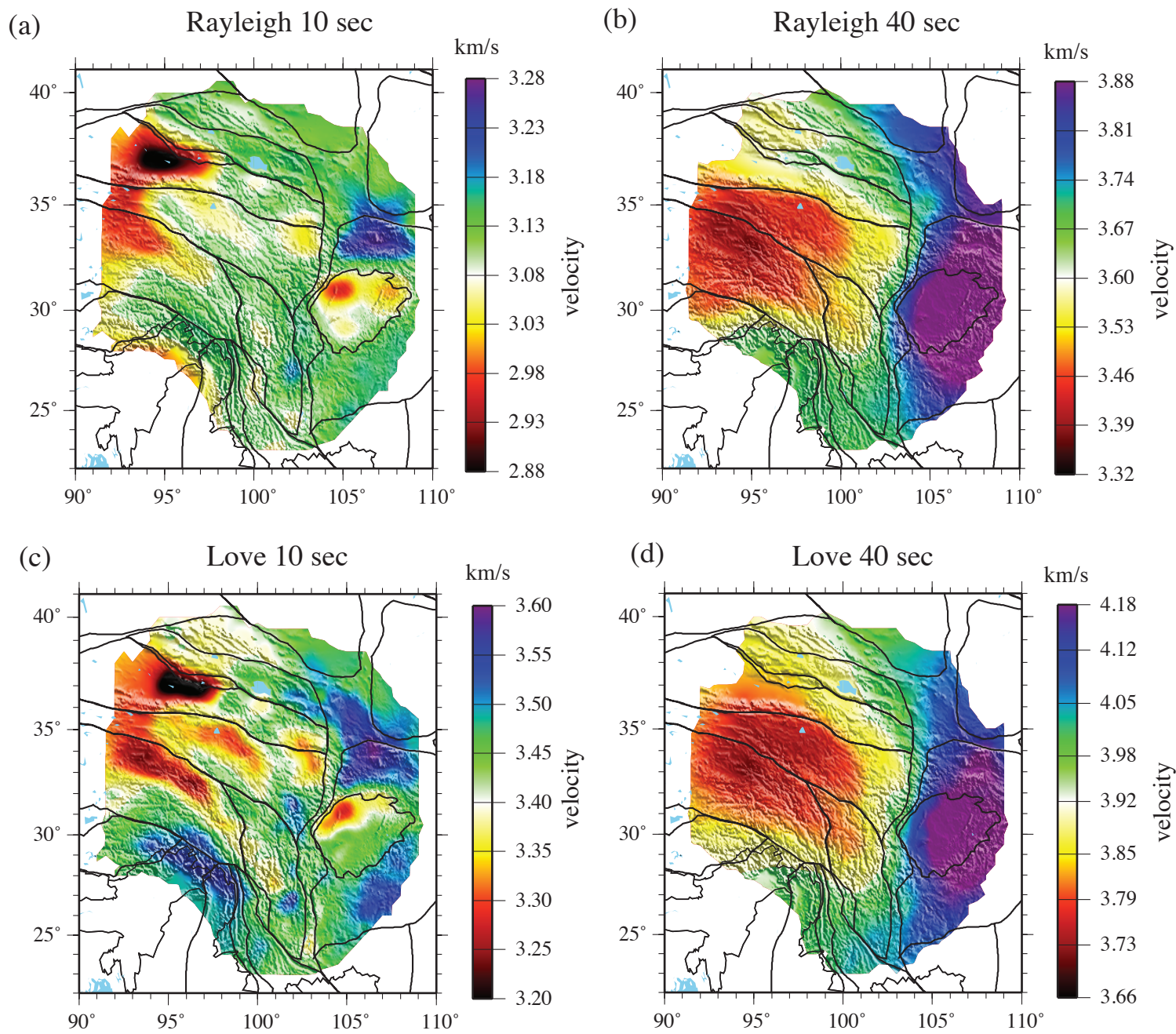


Figure 4

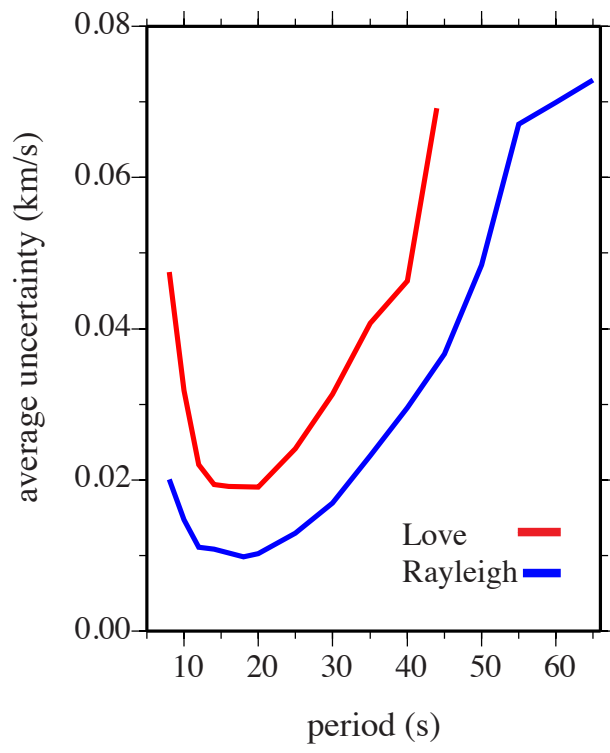


Figure 5

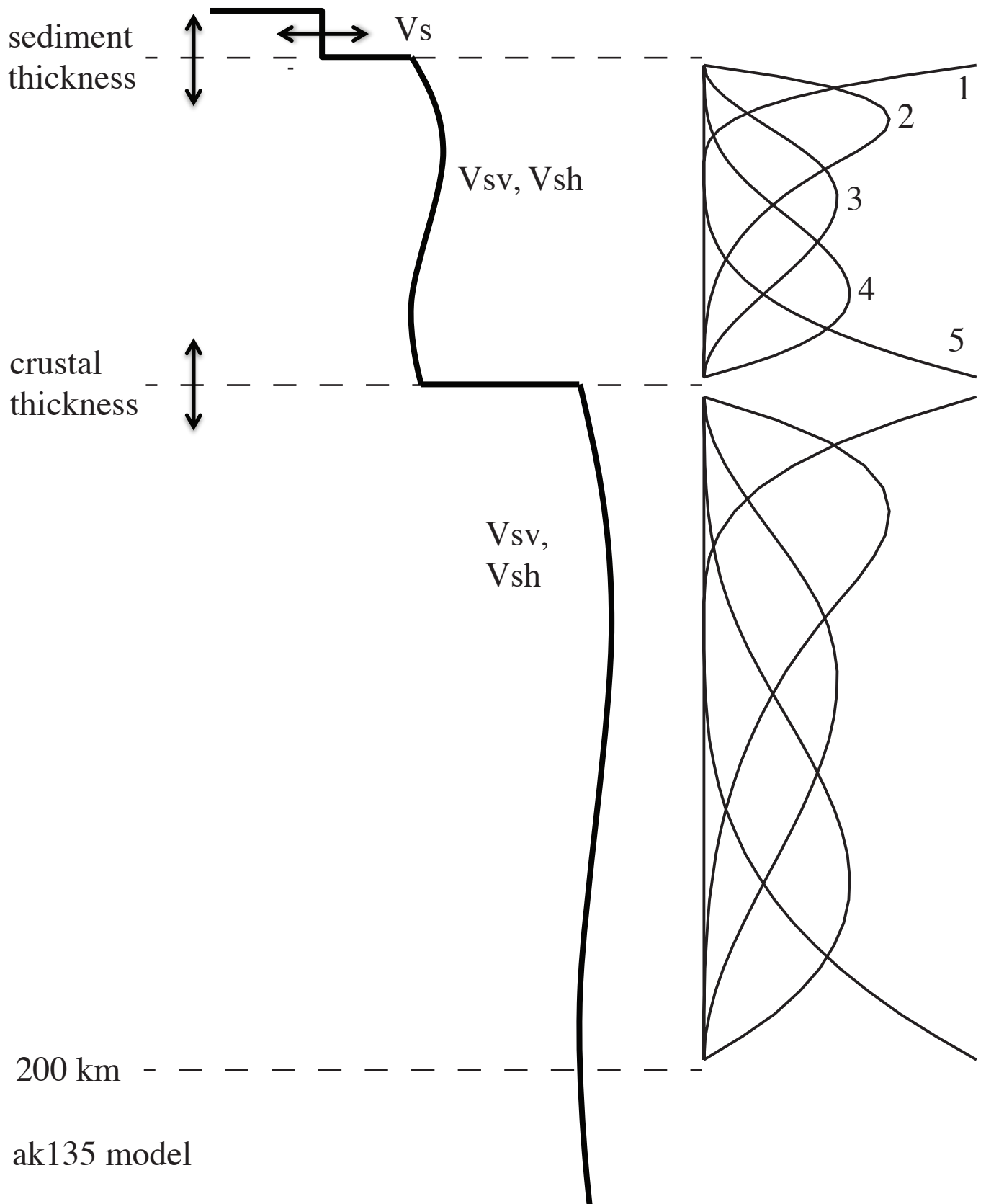


Figure 6

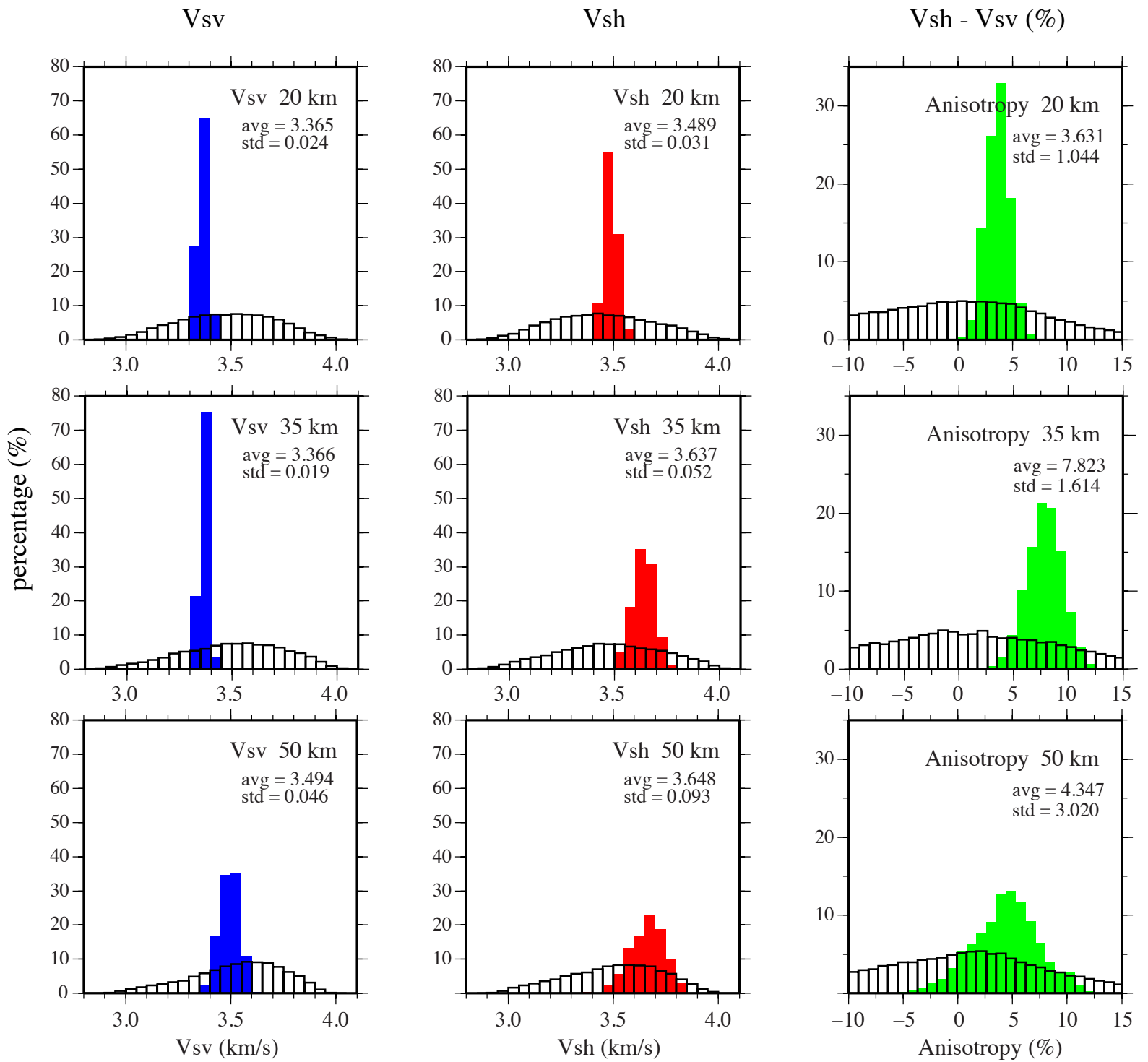


Figure 7

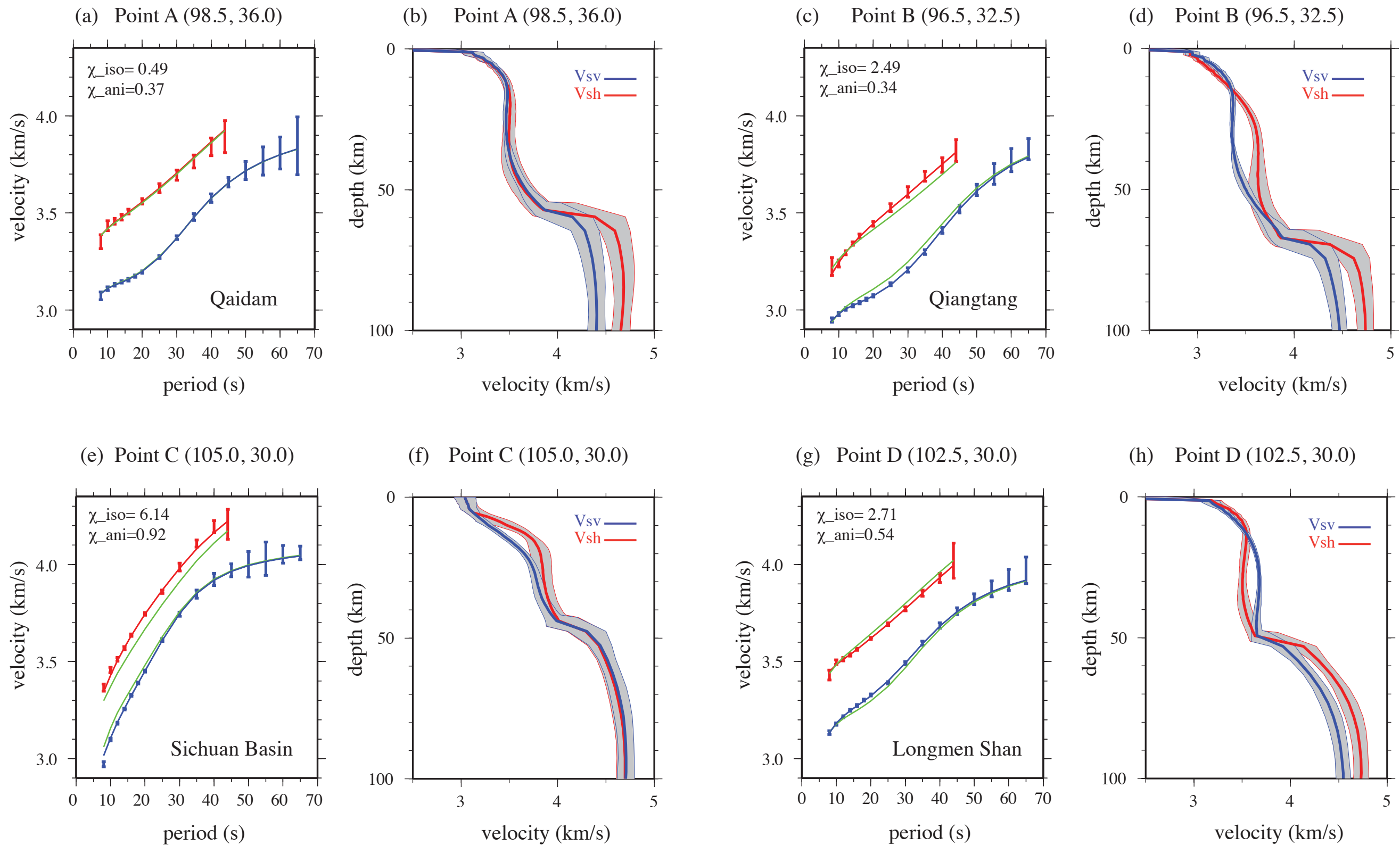


Figure 8

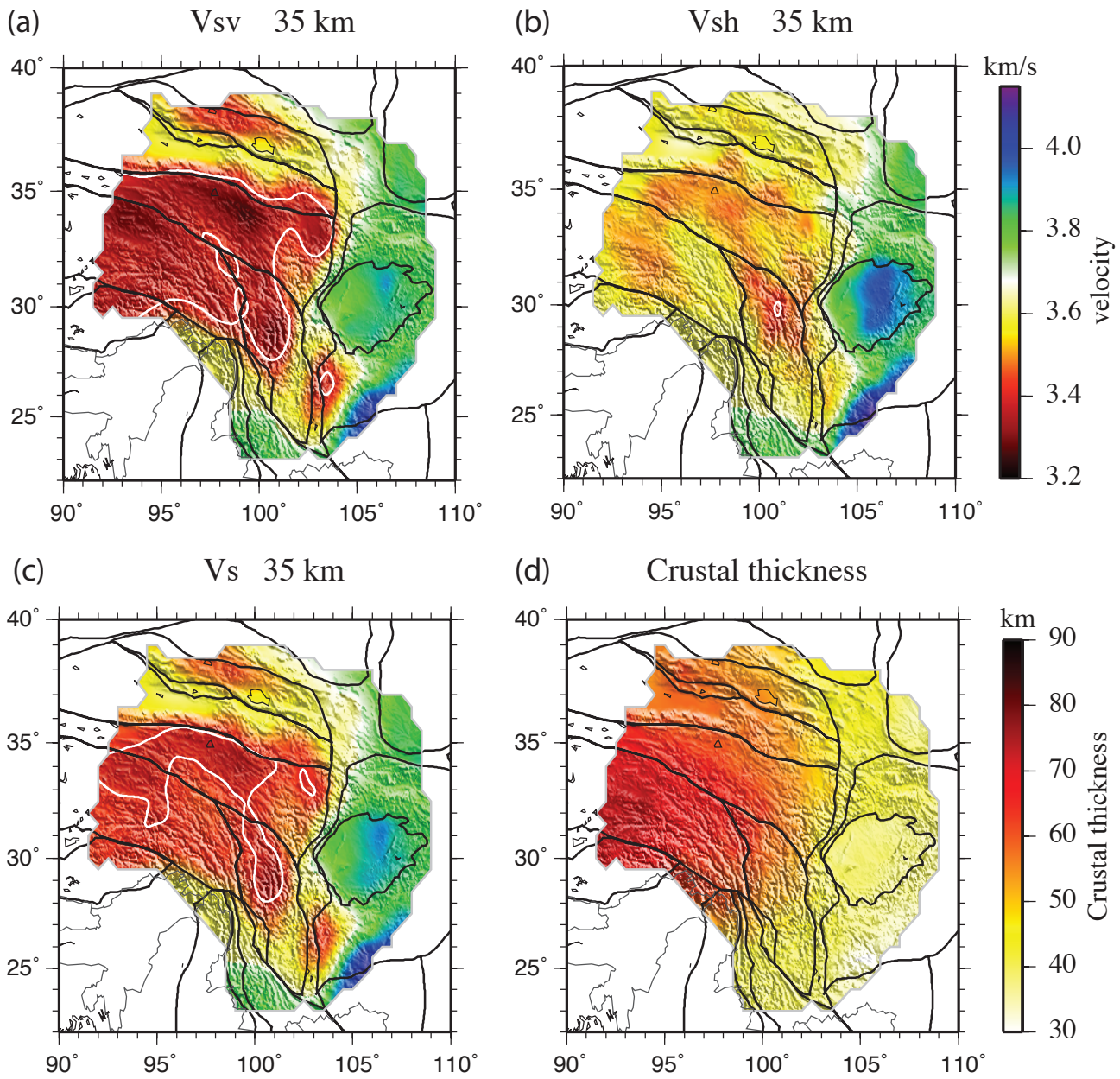


Figure 9

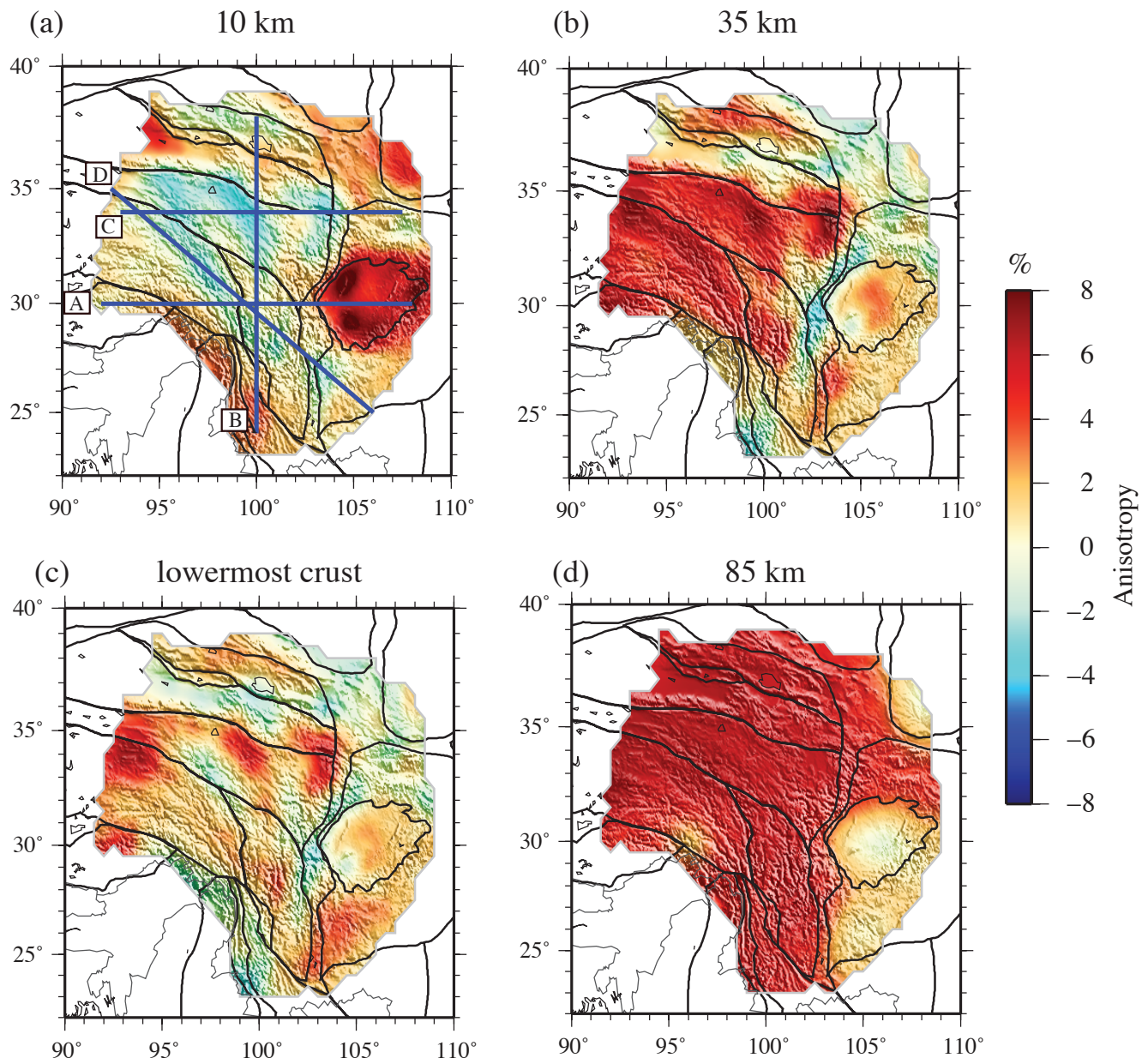


Figure 10

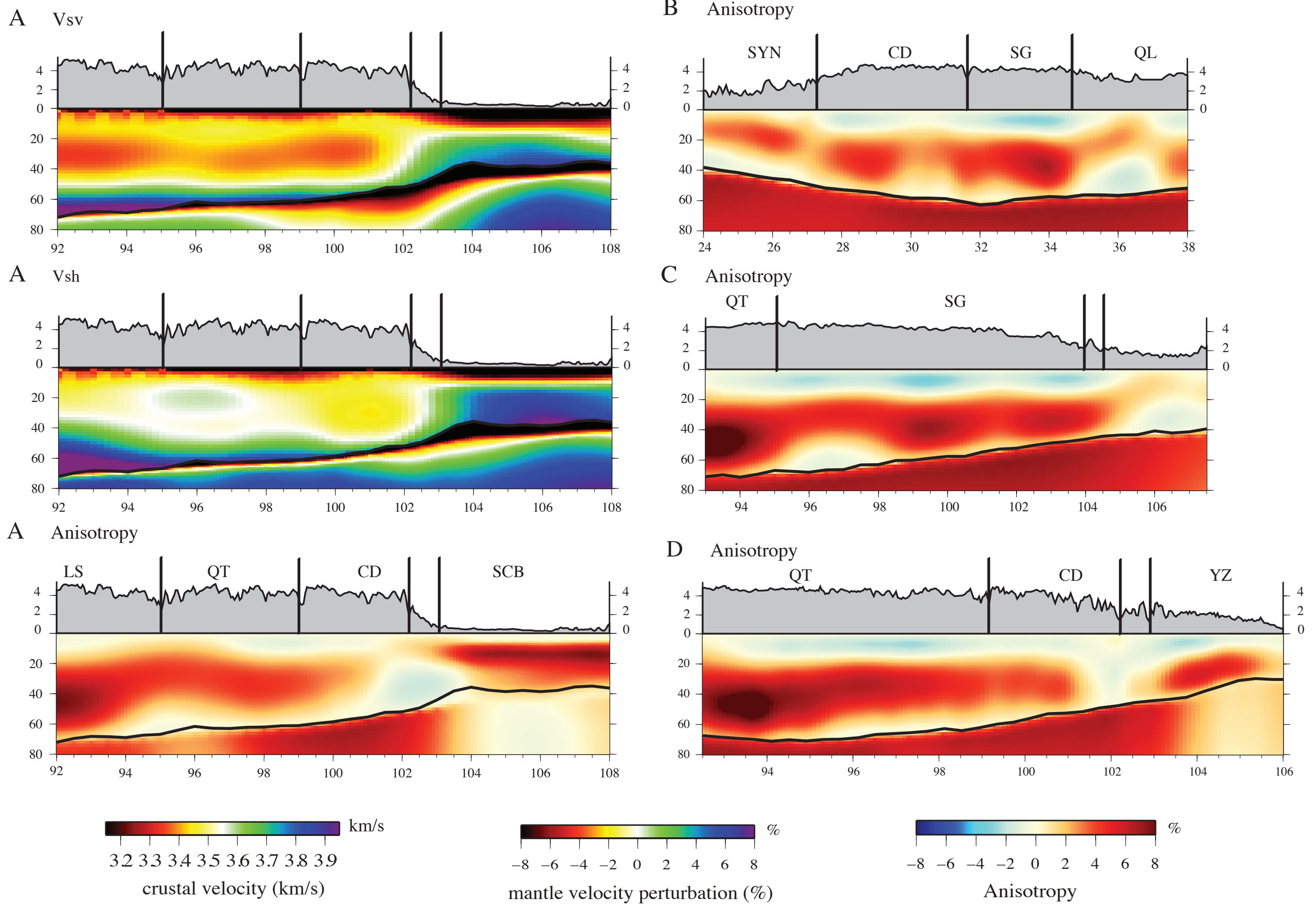


Figure 11

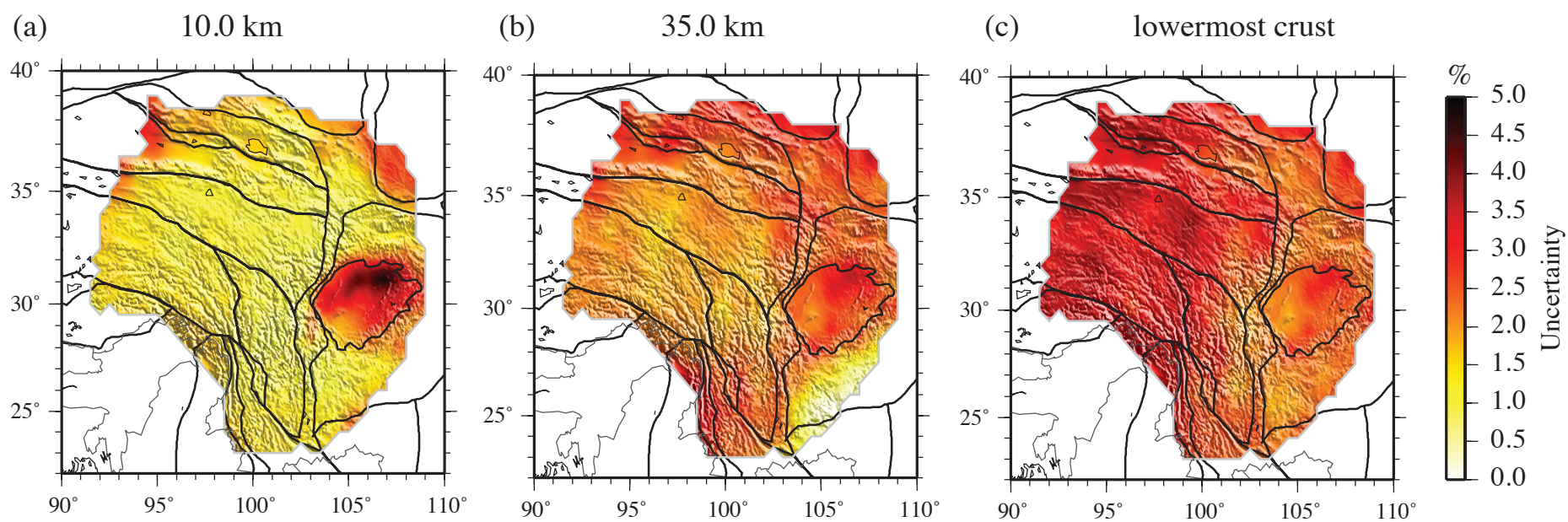


Figure 12

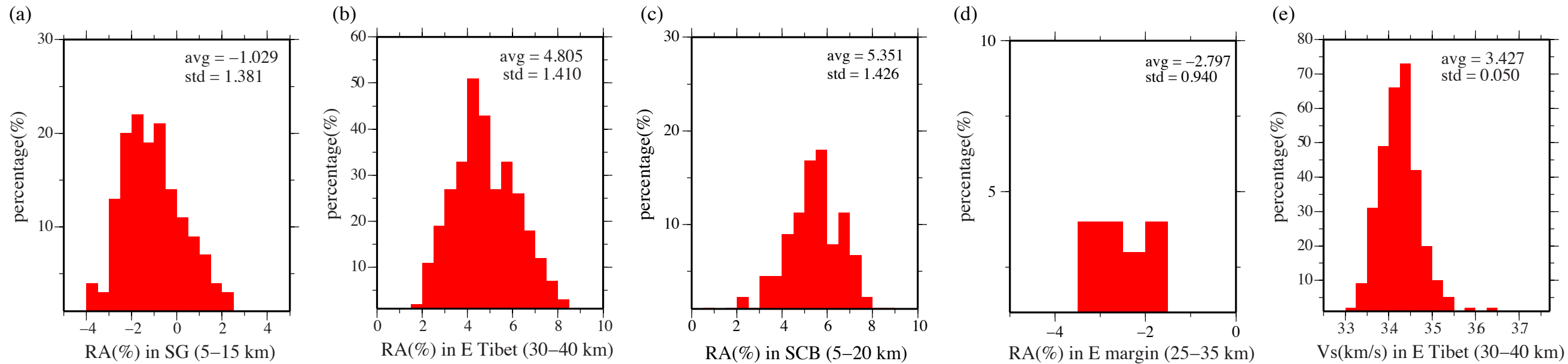


Figure 13

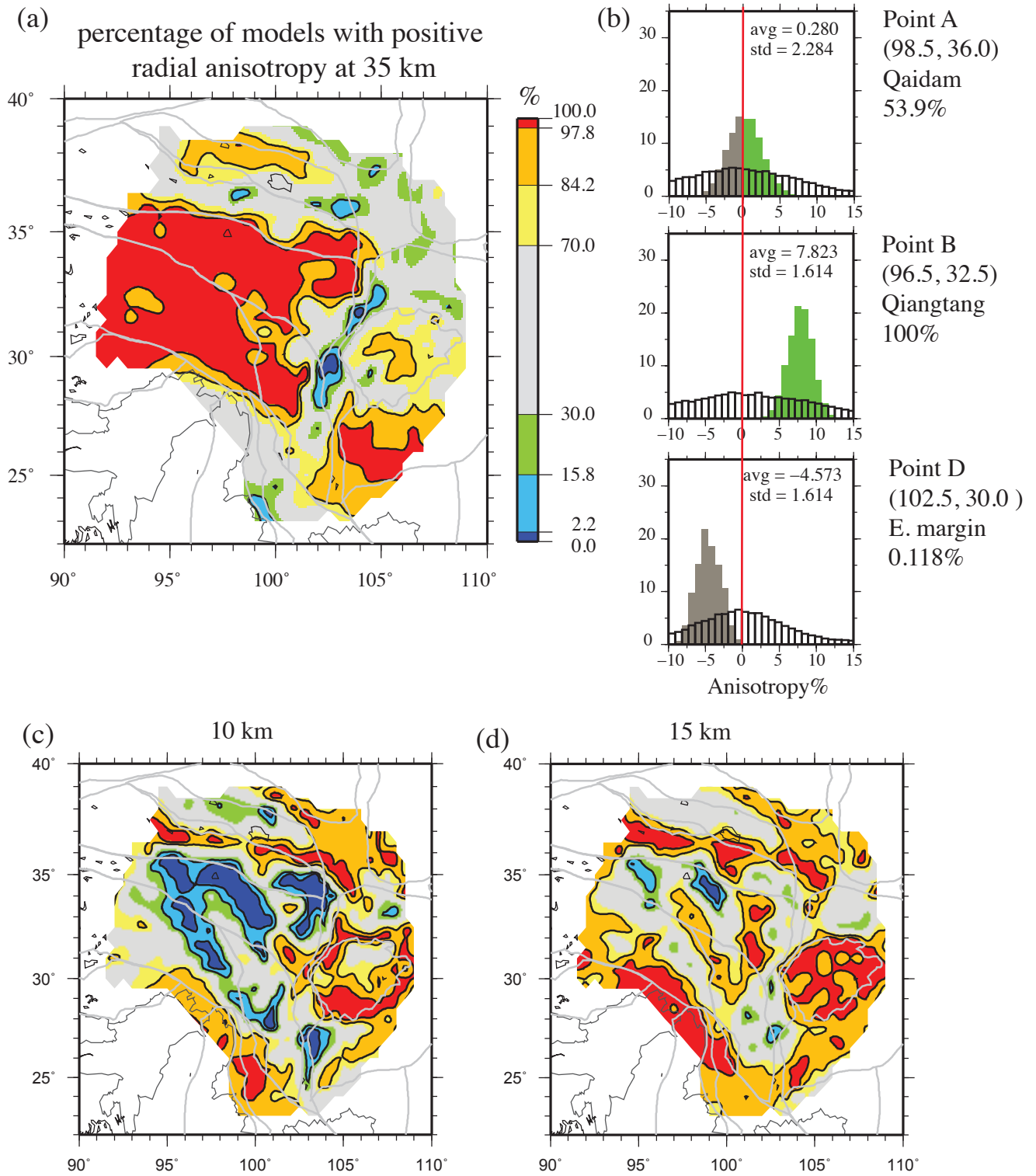
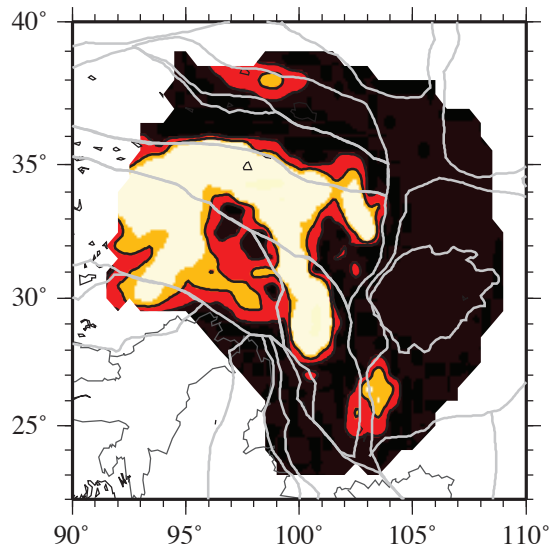


Figure 14

(a) Percentage of models with $V_s > 3.4$ km/s at 35 km



(b) Percentage of models with $V_s < 3.4$ km/s at 35 km

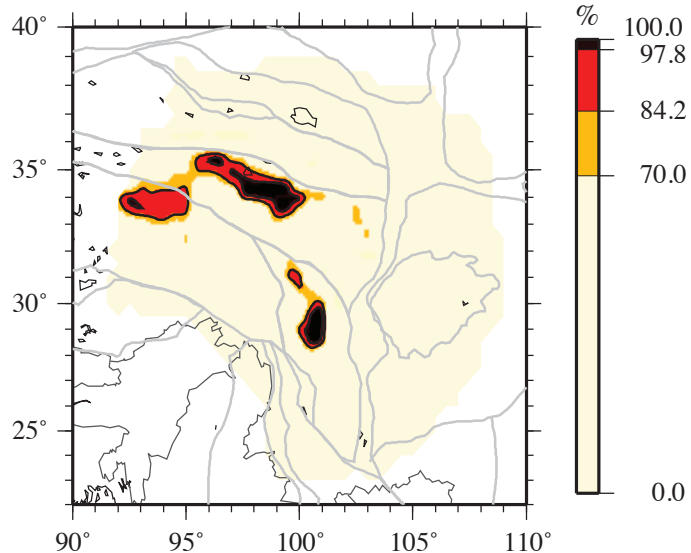


Figure 15

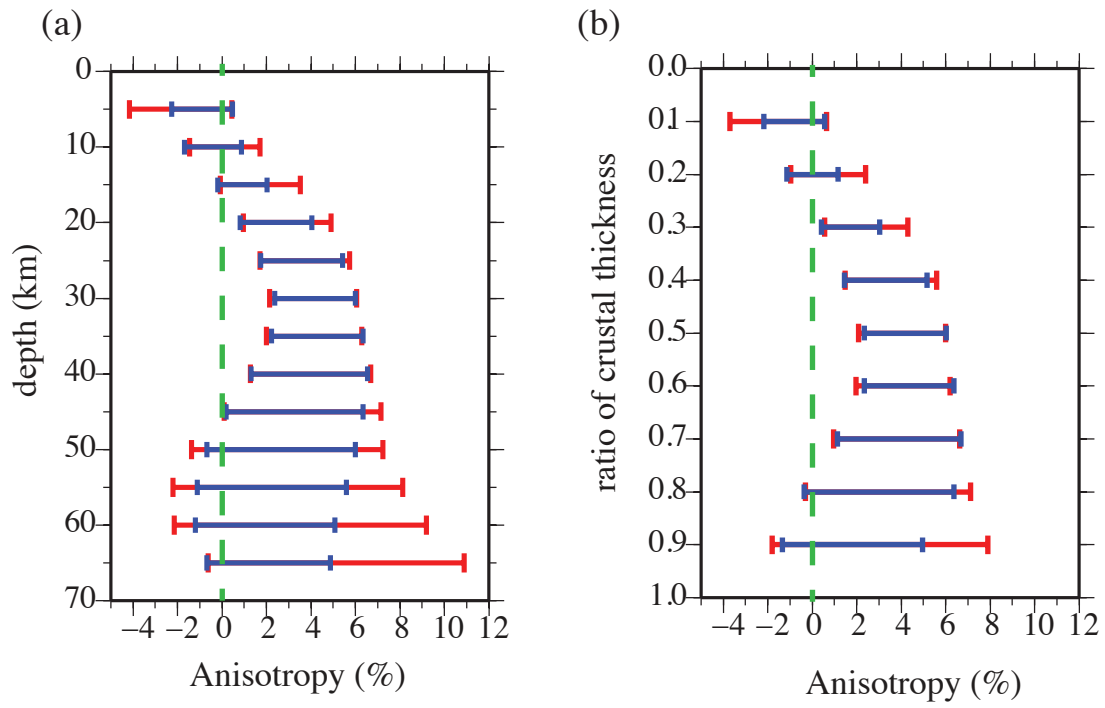


Figure 16

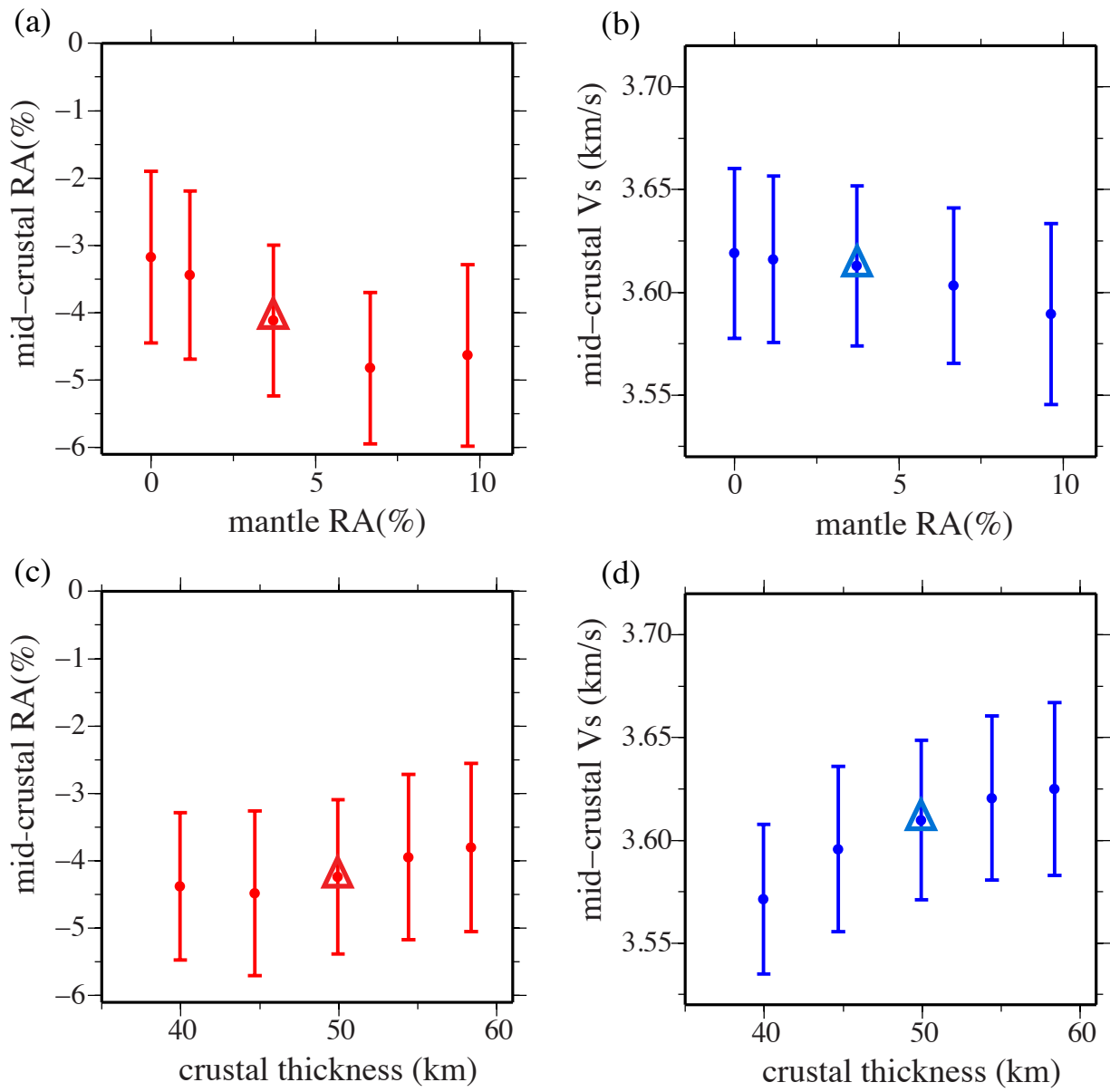


Figure 17

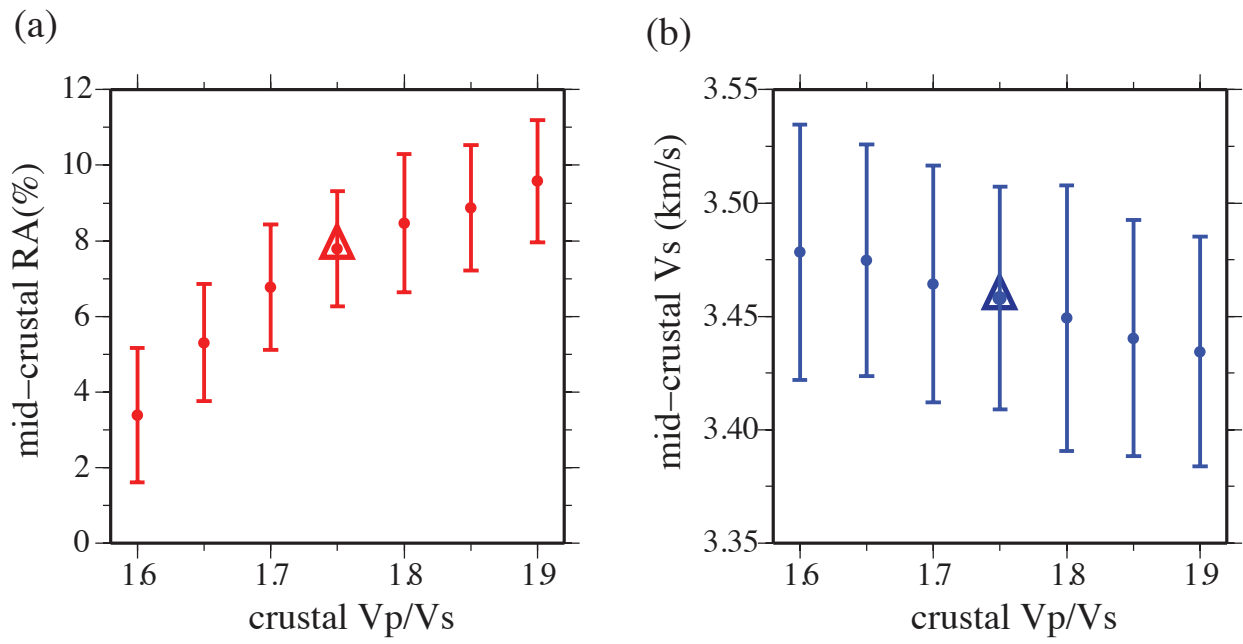


Figure 18

